https://doi.org/10.5194/egusphere-2026-3381
Preprint. Discussion started: 28 July 2026

Constraining anthropogenic CO_2 fluxes in mixed urban source areas using eddy covariance and footprint-informed ecological parameter migration

Jinwen Zhang[1,2], Yongjian Liang[2,3], Yufei Yang[1,2], Chenglei Pei[2,3], Hebiao Huang[4], Bo Huang[5], Xiufeng Lian[1,2], Yingyan Huang[2,3], Yuwen Peng[2,3], Chunlei Cheng[1,2], Cheng Wu[1,2], Zhen Zhou[1,2], and Mei Li[1,2]

[1]College of Environment and Climate, Institute of Mass Spectrometry and Atmospheric Environment, Guangdong Provincial Engineering Research Center for Online Source Apportionment System of Air Pollution, Guangdong–Hongkong–Macau Joint Laboratory of Collaborative Innovation for Environmental Quality, Jinan University, Guangzhou 511443, China
[2]Key Laboratory of Regional Air Quality Monitoring, Ministry of Ecology and Environment, Guangdong, Guangzhou 510308, China
[3]Guangzhou Ecological and Environmental Monitoring Center Station, Guangdong, Guangzhou 510006, China
[4]Guangzhou Academy of Agricultural and Rural Sciences, Guangdong, Guangzhou 510450, China
[5]Guangzhou Hexin Instrument Co., Ltd., Guangdong, Guangzhou 510530, China

Correspondence: Mei Li (limei@jnu.edu.cn)

Abstract. Urban net CO_2 fluxes measured by eddy covariance (EC) cannot be treated as anthropogenic emissions without biogenic constraints, because they integrate fossil-fuel sources, biogenic processes, human respiration, and changing footprints. Existing partitioning approaches often require isotopes, tracers, multi-species fluxes, or clean vegetation/emission sectors unavailable at many urban sites. We developed a footprint-informed ecological parameter-migration framework to constrain anthropogenic CO_2 fluxes (F_{ff}) in mixed urban source areas of Guangzhou, a humid subtropical megacity. A highly vegetated, weakly disturbed suburban donor site provided ecological parameters, which were transferred to a mixed urban target site using dynamic footprints and footprint-weighted enhanced vegetation index (EVI_{fp}). The migrated parameters produced plausible diurnal and seasonal gross primary productivity (GPP) and ecosystem respiration (R_{eco}), supporting the donor–target constraint. At the target site, daytime biogenic uptake masked anthropogenic emissions and occasionally drove net CO_2 flux toward neutral or weakly negative values. After subtracting R_{eco}, GPP, and human respiration, F_{ff} remained consistently positive throughout the day (1.80–5.14 μmol m^{-2} s^{-1}). F_{ff} showed morning and evening peaks consistent with NO_x, CO, wind-sector source areas, and traffic indicators, while footprint-aligned inventories provided

https://doi.org/10.5194/egusphere-2026-3381
Preprint. Discussion started: 28 July 2026

magnitude context and suggested spatial-proxy mismatch in a high-population urban functional zone with relatively low on-site combustion. Uncertainty was dominated by GPP light-response structure, with smaller effects from other perturbations. These results demonstrate the feasibility of extracting footprint-scale F_{ff} from mixed urban source areas using conventional EC, remote-sensing, and footprint data where isotopic or multi-species flux observations are unavailable.

1 Introduction

Urban CO_2 monitoring increasingly needs to determine not only how much CO_2 cities emit, but also how observed CO_2 signals are jointly shaped by fossil-fuel combustion, biogenic processes, human respiration, and atmospheric transport (Sargent et al., 2018; Zhang et al., 2026). This distinction is particularly important in urban landscapes where green space, roads, buildings, residential activity, and water bodies are highly interwoven. Although cities generally act as net CO_2 sources, urban vegetation can substantially modulate local CO_2 exchange and can partially offset, mask, or reshape the diurnal and seasonal signatures of anthropogenic emissions (Velasco and Roth, 2010; Nordbo et al., 2012; Hardiman et al., 2017; Miller et al., 2020). Therefore, net CO_2 exchange observed in urban environments cannot be directly interpreted as fossil-fuel or anthropogenic CO_2 emissions unless biogenic processes are explicitly constrained (Wu et al., 2022; Soininen et al., 2025).

Eddy covariance (EC) is one of the few approaches capable of directly measuring surface-atmosphere CO_2 exchange at high temporal resolution (Baldocchi, 2003; Velasco and Roth, 2010). It has been widely used to quantify ecosystem carbon exchange and has increasingly been applied to urban CO_2 flux observations (Järvi et al., 2012; Liu et al., 2012; Matthews and Schume, 2022; Ueyama and Takano, 2022; Horne et al., 2026). Urban EC studies have shown that CO_2 fluxes often exhibit pronounced diurnal, seasonal, and source-area dependence, reflecting the combined influences of traffic activity, building energy use, vegetation phenology, land-cover composition, and meteorological conditions (Velasco et al., 2013; Ward et al., 2015; Pérez-Ruiz et al., 2020). However, EC directly measures the net exchange of all CO_2 sources and sinks within a dynamic flux footprint (Menzer and McFadden, 2017; Lee et al., 2021). In

https://doi.org/10.5194/egusphere-2026-3381
Preprint. Discussion started: 28 July 2026

mixed urban source areas, a daytime reduction or even reversal of net CO_2 flux does not necessarily indicate weakened anthropogenic emissions, but may at least partly reflect enhanced photosynthetic uptake (Sargent et al., 2018; Wu et al., 2022). Thus, the key challenge for urban EC studies is not whether CO_2 fluxes can be observed, but how net fluxes can be partitioned into physically interpretable anthropogenic and biogenic components.

Previous studies have attempted to partition urban EC net CO_2 fluxes using inventories, statistical methods, source-area sectors, and tracers. Early work combined EC observations with bottom-up inventories to evaluate urban CO_2 emissions or attribute them to traffic and domestic heating (Matese et al., 2009). Such comparisons provide useful magnitude context, but inventory-based interpretation alone cannot separate the biogenic and anthropogenic components embedded in EC net fluxes at the dynamic footprint scale. Menzer and McFadden (2017) statistically partitioned multi-year urban net CO_2 fluxes into biogenic and anthropogenic components, and Lee et al. (2021) incorporated footprint-weighted land cover and temporal subsets to separate gross primary productivity (GPP), ecosystem respiration (R_{eco}), vehicle emissions, and building emissions. More recently, O_2:CO_2, CO, radiocarbon (^{14}C), carbonyl sulfide (COS), and multi-species EC measurements have provided stronger constraints on urban CO_2 flux partitioning (Ishidoya et al., 2020; Wu et al., 2022; Soininen et al., 2025; Hilland et al., 2025; Kunz et al., 2026). In particular, Soininen et al. (2025) fitted ecological light-response parameters in a vegetation-dominated sector and applied them to a street-sector footprint, obtaining residual anthropogenic CO_2 fluxes comparable to bottom-up traffic emissions. This provides an important example in which parameters derived from a relatively clean ecological source area can be used to estimate biogenic contributions in a mixed or emission-dominated source area. Beyond source partitioning, such footprint-scale anthropogenic flux estimates can also help evaluate whether proxy-based gridded inventories allocate emissions realistically within heterogeneous urban functional zones, where population density, night-time lights, or road density may not scale with local combustion intensity (Gately and Hutyra, 2017; Squires et al., 2020; Wu et al., 2022).

Nevertheless, these approaches remain difficult to generalize. Methods based on

https://doi.org/10.5194/egusphere-2026-3381
Preprint. Discussion started: 28 July 2026

^{14}C, COS, O_2:CO_2, or multi-species EC usually require additional instrumentation, sampling, or calibration infrastructure (Ishidoya et al., 2020; Soininen et al., 2025; Kunz et al., 2026), whereas statistical and sector-transfer approaches often require clearly separated vegetation-dominated and emission-dominated source areas around the tower (Menzer and McFadden, 2017; Lee et al., 2021; Soininen et al., 2025). For cities equipped only with conventional EC, meteorological, remote-sensing, and land-cover data, this limitation is particularly important where vegetation, roads, buildings, and water bodies are tightly mixed and no clean vegetation sector is available. In such settings, the partitioning problem becomes: how can the biogenic component be robustly estimated at the dynamic EC-footprint scale and removed from the net flux?

Conventional ecosystem flux partitioning usually estimates R_{eco} from nighttime temperature responses and GPP from daytime light-response curves (Reichstein et al., 2005; Lasslop et al., 2010). Directly fitting these ecological parameters at an urban EC site is problematic because fluxes may be contaminated by traffic, building-related emissions, human activity, and storage changes. Fixed-buffer vegetation indices or land-cover fractions also ignore the continuous variation of EC source areas with wind direction, turbulence, and atmospheric stability. Flux footprint models can link each flux observation to its actual contributing source area (Kljun et al., 2015), while the enhanced vegetation index (EVI) can represent canopy greenness, vegetation activity, and photosynthetic potential (Huete et al., 2002; Mahadevan et al., 2008). However, dynamic footprints and vegetation indices alone do not identify the baseline ecological response at the target site, because the target-site net flux remains a superposition of biogenic exchange and anthropogenic emissions. This motivates the hypothesis tested here: ecological parameters obtained from a nearby donor site with weaker anthropogenic disturbance may provide the missing ecological response reference and can be transferred to a mixed urban target site when constrained by vegetation amount and activity within the dynamic target footprint.

Such cross-site parameter migration should avoid mechanically imposing donor-site parameters on the target footprint. Ecosystem-scale light-response parameters are apparent canopy-scale quantities controlled by canopy structure, vegetation amount, phenology, and environmental conditions, rather than fixed leaf-level constants (Sellers,

https://doi.org/10.5194/egusphere-2026-3381
Preprint. Discussion started: 28 July 2026

1985; Myneni and Williams, 1994; Huete et al., 2002). This provides the basis for treating donor-site parameters as a same-region ecological-response reference when donor and target footprints share broadly similar climatic and vegetation backgrounds. Similar logic is used in light-use-efficiency and VPRM-style models, where vegetation indices are combined with environmental scalars to estimate photosynthetic uptake and urban biogenic CO_2 fluxes (Monteith, 1972; Running et al., 2004; Xiao et al., 2004; Mahadevan et al., 2008; Gourdji et al., 2022). In this framework, footprint-weighted EVI links remotely sensed vegetation activity to the actual EC source area (Huete et al., 2002; Kljun et al., 2015; Järvi et al., 2019). For GPP, this constraint is relatively direct because EVI tracks photosynthetically active vegetation amount and canopy greenness, and is therefore closely linked to canopy light-absorbing capacity. For R_{eco}, EVI is used more cautiously as a footprint-scale vegetated/pervious-surface mask and capacity-normalization factor, rather than as a direct physiological driver. This treatment is consistent with urban biogenic CO_2 models that use vegetation fractions or remote-sensing vegetation proxies together with meteorological and urban-surface modifiers to represent vegetation and soil respiration (Järvi et al., 2019; Hardiman et al., 2017; Wu et al., 2021), and with urban soil-respiration measurements showing substantial respiration from vegetated and managed pervious cover types (Decina et al., 2016). Therefore, both respiration and light-response parameter migration are treated as constrained approximations and evaluated through sensitivity analyses.

Based on this gap and rationale, we develop a footprint-informed ecological parameter migration framework to separate biogenic and anthropogenic CO_2 fluxes from urban EC observations in Guangzhou, China. Guangzhou is a humid subtropical megacity characterized by high population density, strong traffic activity, and substantial urban vegetation, making it a representative testbed for partitioning CO_2 fluxes in mixed urban source areas. Our previous concentration-based study in Guangzhou showed that urban CO_2 variability is jointly influenced by anthropogenic emissions, biogenic exchange, and sea–land breeze transport, and that vegetation uptake during the growing season can weaken the apparent fossil-fuel CO_2 signal (Zhang et al., 2026). Compared with concentration observations, EC can provide a more direct constraint on local surface-atmosphere exchange, but only if the biogenic

https://doi.org/10.5194/egusphere-2026-3381
Preprint. Discussion started: 28 July 2026

contribution within the flux footprint can be estimated and removed.

To address this challenge, we use paired EC observations from two sites in Guangzhou in a donor–target design. The Conghua (CH) site is located in a highly vegetated area with weak anthropogenic activity and is used as a relatively clean ecological donor site. The Panyu (PY) site is located in a mixed urban source area composed of vegetation, roads, buildings, and water bodies and is used as the urban target site. We first constrain R_{eco} and GPP light-response parameters at CH, and then migrate these ecological parameters to PY using dynamic flux footprints and footprint-weighted EVI. After subtracting R_{eco}, GPP, and human respiration, we define the remaining flux as F_{ff}, an operational estimate of footprint-scale anthropogenic CO_2 flux. We then evaluate this interpretation using independent pollutant, source-area, traffic-activity, and inventory-magnitude evidence, while also assessing the dominant sources of uncertainty.

This study addresses three questions: (i) can footprint-weighted vegetation activity provide an ecologically consistent constraint for migrating ecological parameters from a relatively clean donor site to a heterogeneous urban target footprint; (ii) how do partitioned biogenic and anthropogenic components jointly shape net CO_2 exchange within a mixed urban footprint in a humid subtropical megacity; and (iii) do the operationally defined F_{ff} estimates show temporal and source-area patterns consistent with footprint-scale anthropogenic activity, provide useful context for inventory spatial allocation, and remain robust under key uncertainty sources? By answering these questions, this study provides a transferable framework for partitioning urban CO_2 source and sink components using conventional EC, remote sensing, and flux footprints in cities without isotopic or multi-species flux measurements. It also offers footprint-scale observational constraints for interpreting anthropogenic emissions, biogenic modulation, and inventory spatial allocation in mixed urban source areas.

2 Data and methods

2.1 Study sites

This study used eddy covariance (EC) observations from two sites in Guangzhou, China: Panyu (PY) and Conghua (CH). Both sites are part of an urban high-precision

https://doi.org/10.5194/egusphere-2026-3381
Preprint. Discussion started: 28 July 2026

greenhouse-gas monitoring network and are equipped with high-precision greenhouse-gas concentration, CO_2 flux, and meteorological measurement systems. The site-selection strategy and basic observational information have been reported by Zhang et al. (2026). Guangzhou has a humid subtropical monsoon climate (according to the Köppen climate classification), with a mean annual temperature of 23.7 °C and mean annual precipitation of 1933.6 mm. The PY site (113.380° E, 23.037° N) is located in the Guangzhou Higher Education Mega Center, where urban green space, roads, buildings, water bodies, and dense human activity are closely interwoven. The CH site (113.777° E, 23.747° N) is located near Liuxi River National Forest Park, where population density is low and vegetation cover is high (Fig. 1). A two-dimensional flux-footprint model centered on each tower and 10 m land-cover data show that the PY footprint is composed of 46 % impervious surface, 44 % vegetation, and 10 % water/wetland, with urban forest accounting for 60 % of the vegetated area (Kljun et al., 2015; Zhang et al., 2025). The CH footprint is composed of 2 % impervious surface, 86 % vegetation, and 12 % water/wetland, with urban forest accounting for 96 % of the vegetated area. Urban forests at both sites are dominated by evergreen broadleaf trees, including Bauhinia, eucalyptus, kapok, and autumn maple. The key contrast between the two sites is therefore not climate zone, but vegetation cover, urbanization intensity, and anthropogenic-activity background.

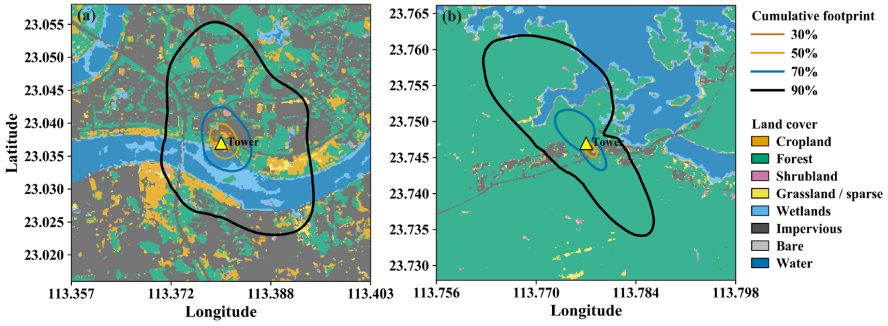

Figure 1. Two-dimensional climatological footprint contours over land-cover classes at the PY and CH sites. Panels **(a)** and **(b)** show the PY and CH sites, respectively. Background land-cover classes were derived from the 2023 global 10 m land-cover product GLC_FCS10 (Zhang et al., 2025). The footprint model was evaluated on a 10 m spatial grid to match the land-cover data. The overlaid contours represent cumulative footprint contributions of 30 %, 50 %, 70 %, and 90 %, and yellow triangles mark the tower locations.

https://doi.org/10.5194/egusphere-2026-3381
Preprint. Discussion started: 28 July 2026

Table S3 and Fig. S6 show that CH and PY have similar seasonal phases in temperature and shortwave radiation, although PY has a warmer urban microclimatic background and the month-to-month consistency in vapor pressure deficit (VPD) is relatively weak. We therefore do not assume identical microclimatic conditions or identical carbon-exchange magnitudes at the two sites. Rather, the site pair provides a donor–target contrast under the same regional climate and broadly similar vegetation background, with CH representing weaker anthropogenic disturbance and PY representing a mixed urban source area.

2.2 EC flux observations and quality control

EC CO_2 fluxes were measured from tall tower platforms at both sites. At PY, the EC system consisted of an open-path CO_2/H_2O analyzer (LI-7500DS, LI-COR Inc., USA) and a three-dimensional sonic anemometer (WindMaster Pro, Gill Inc., UK), installed at 48 m. At CH, an open-path IRGASON system (Campbell Scientific Inc., USA), integrating a three-dimensional sonic anemometer and an infrared CO_2/H_2O analyzer, was installed at 40 m. Based on a 10 m canopy-height product (Lang et al., 2023) and vector building-height data (https://lbs.amap.com, last access: 25 May 2026), the mean effective roughness-element heights within the PY and CH footprints were 13.1 and 15.2 m, respectively. The measurement heights at both sites exceeded twice the mean roughness-element height (Z_H, m), supporting their representativeness for turbulent fluxes over the study source areas (Rotach, 1999; Grimmond and Oke, 1999; Velasco and Roth, 2010). The observation period extended from 1 January 2023 to 30 April 2025.

During the observation period, the EC systems recorded CO_2/H_2O concentration, three-dimensional wind components, air temperature, relative humidity, and related variables at 10 Hz. Half-hourly fluxes were calculated from the covariance between vertical wind speed and CO_2 mole fraction. Flux processing followed standard EC procedures, including Webb-Pearman-Leuning (WPL) density correction, double coordinate rotation, and 30 min detrending (Webb et al., 1980; Sabbatini et al., 2018).

To ensure data reliability, we applied a stepwise quality-control procedure.

https://doi.org/10.5194/egusphere-2026-3381
Preprint. Discussion started: 28 July 2026

Records flagged for extreme weather, instrument maintenance, or obvious malfunction were removed. Low-turbulence nighttime periods were filtered using the friction velocity (u*) threshold method implemented in REddyProc (Papale et al., 2006; Wutzler et al., 2018). Non-stationary fluxes were excluded using the stationarity test of Foken et al. (2004), and despiking was then applied. After quality control, the valid-data fractions for net CO_2 fluxes were 51.7 % at PY and 54.5 % at CH, comparable to common ranges in urban EC studies (Matthews and Schume, 2022). The detailed quality-control procedure and retention rates are given in Sect. S1. The net fluxes were subsequently corrected for storage following the procedure described in Sect. S2 (Aubinet et al., 2001; Kooijmans et al., 2017; Kohonen et al., 2020; Soininen et al., 2025). The daily mean storage fluxes were 0.03 and 0.04 μmol m^{-2} s^{-1} at PY and CH, respectively, much smaller than the measured fluxes. All subsequent analyses therefore used storage-corrected net CO_2 fluxes. Unless otherwise stated, storage-corrected fluxes, footprint calculations, ecological parameter fitting, parameter migration, and F_{ff} propagation were performed at the native 30 min time step. These results were aggregated to hourly means for diurnal and cross-variable analyses, and further summarized at daily, monthly, or seasonal scales where needed.

2.3 CO_2 flux partitioning framework

The net CO_2 flux observed by an urban EC system integrates multiple source and sink processes within the footprint, including fossil-fuel emissions, human respiration, ecosystem respiration, biogenic uptake, and changes in air-column storage (Wu et al., 2022; Soininen et al., 2025; Hilland et al., 2025). The storage-corrected flux is defined as:

$$F_{cr}(t) = F_{mz}(t) + F_{st}(t) \quad (1)$$

Here F_{cr} is the storage-corrected CO_2 flux (μmol m^{-2} s^{-1}), F_{mz} is the measured net CO_2 flux after quality control (μmol m^{-2} s^{-1}), and F_{st} is the storage flux (μmol m^{-2} s^{-1}). F_{cr} was then partitioned into the following components:

$$F_{cr}(t) = F_{ff}(t) + F_{hu}(t) + R_{eco}(t) - GPP(t) \quad (2)$$

Here F_{ff} is operationally defined as the anthropogenic CO_2 flux remaining after

https://doi.org/10.5194/egusphere-2026-3381
Preprint. Discussion started: 28 July 2026

subtracting ecosystem respiration (R_{eco}), gross primary productivity (GPP), and human respiration (F_{hu}) from the storage-corrected net flux. F_{hu} is the human-respiration flux, R_{eco} is the sum of plant and soil respiration, and GPP is the amount of CO_2 fixed by photosynthesis. Within the PY footprint, direct fossil-fuel emissions are expected to be dominated by road traffic and related urban activities. Because buildings within the source area mainly rely on externally supplied electricity, on-site building-energy combustion was not explicitly considered (Yang et al., 2025). F_{hu} was estimated from population density and per-capita respiration rate (Sect. S3).

2.4 Ecological flux parameterization at the donor site

Ecological parameters for R_{eco} and GPP were fitted at CH and then migrated to PY as described in Sect. 2.5. The donor-site ecological parameterization followed a two-step framework in which nighttime respiration was fitted first and daytime GPP was then inferred from the light response. This approach has been widely used for partitioning EC-based NEE into ecosystem respiration and photosynthetic uptake (Reichstein et al., 2005; Lasslop et al., 2010). Nighttime ecosystem respiration (PAR < 10 μmol m^{-2} s^{-1}) was represented using a simplified Q10 temperature-response equation:

$$R_{eco}(t) = R_c(t) Q_{10}^{T_a(t)/10} \quad (3)$$

Here T_a is the driving air temperature (°C), Q10 is the temperature-sensitivity coefficient and represents the relative increase in respiration rate for a 10 °C temperature increase, and R_c is the base level of respiration (μmol m^{-2} s^{-1}). Because daytime ecosystem respiration may be suppressed by light (Wehr et al., 2016; Keenan et al., 2019), daytime respiration was further represented as:

$$R_{eco,day}(t) = R_{eco}(t)\left[1 - \beta \frac{PAR(t)}{K_L + PAR(t)}\right] \quad (4)$$

Here $R_{eco,day}$ is the light-modified daytime ecosystem respiration (μmol m^{-2} s^{-1}), β is the maximum inhibition fraction, K_L is the light-inhibition half-saturation constant (μmol photon m^{-2} s^{-1}), and PAR is photosynthetically active radiation (μmol photon m^{-2} s^{-1}). Because PAR was not measured directly, it was converted from shortwave radiation (Sects. S4 and S7). The baseline setting used β = 0.15 and K_L = 600 μmol

https://doi.org/10.5194/egusphere-2026-3381
Preprint. Discussion started: 28 July 2026

photon m^{-2} s^{-1}. A weak daytime-respiration-inhibition scenario, with a lower β (0.10) and a higher K_L (800 μmol photon m^{-2} s^{-1}), was used to evaluate the influence of this assumption on ecological-parameter fitting and F_{ff} estimation.

Daytime GPP was represented using a non-rectangular hyperbolic saturating light-response equation:

$$GPP(t) = \frac{\alpha PAR(t) + P_{max} - \sqrt{(\alpha PAR(t) + P_{max})^2 - 4\theta P_{max}\alpha PAR(t)}}{2\theta} \quad (5)$$

Here α is the initial light-use efficiency, defined as the initial slope of the GPP response to PAR under low-light conditions; P_{max} is the maximum photosynthetic capacity (μmol m^{-2} s^{-1}); and θ is the curvature parameter controlling the transition from the low-light linear segment to the high-light saturation segment. We then used three GPP model structures to evaluate how ecological structural assumptions affect CH-side GPP fitting and PY-side F_{ff} estimation:

(1) Pure saturating structure: the non-rectangular hyperbolic form above was used directly, without temperature stratification or VPD inhibition. All samples satisfying the GPP-fitting criteria were fitted within a single parameter group for α, P_{max}, and θ.

(2) Saturating structure with VPD inhibition: VPD inhibition of maximum photosynthetic capacity was introduced into the non-rectangular hyperbolic form to test the influence of atmospheric dryness stress (Lasslop et al., 2010). Specifically, P_{max} was replaced by an effective maximum photosynthetic capacity regulated by VPD:

$$P_{max,VPD} = P_{max} \times f_{VPD} \quad (6)$$

$$f_{VPD} = exp[-k_{VPD} max(0, VPD - VPD_0)] \quad (7)$$

Here $P_{max,VPD}$ is the VPD-regulated effective maximum photosynthetic capacity (μmol m^{-2} s^{-1}), f_{VPD} is the VPD inhibition factor, VPD is vapor pressure deficit (kPa), k_{VPD} is the VPD inhibition coefficient (kPa^{-1}), and VPD_0 is the reference threshold above which inhibition is applied; VPD_0 was set to 1.0 kPa. No additional inhibition was applied when VPD was below 1.0 kPa. Above this threshold, maximum photosynthetic capacity declined exponentially with increasing VPD. VPD calculation is described in Sect. S4.

(3) Saturating structure with temperature stratification: instead of adding a

https://doi.org/10.5194/egusphere-2026-3381
Preprint. Discussion started: 28 July 2026

continuous temperature-response function to the GPP equation, GPP-fitting samples were grouped by air temperature (T_a), and α, P_{max}, and θ were fitted separately within each temperature group. The baseline analysis used Scheme A, in which the CH-side GPP-fitting samples were divided into low-, mid-, and high-temperature groups according to the tertiles of T_a:

$$q_1 = quantile(T_a, 1/3) \quad (8)$$

$$q_2 = quantile(T_a, 2/3) \quad (9)$$

Here T_a is air temperature (°C), and q_1 and q_2 are the one-third and two-third quantiles of air temperature in the fitting samples. The low-temperature group is $T_a < q_1$, the mid-temperature group is $q_1 \le T_a < q_2$, and the high-temperature group is $T_a \ge q_2$. This treatment represents differences in light-response parameters under different thermal states while avoiding an additional continuous temperature-response function under limited data and complex urban source-area conditions. To test the sensitivity to temperature-boundary selection, we used Scheme B as a structural sensitivity scenario. Scheme B kept the equations, fitting windows, and screening criteria unchanged, but expanded the mid-temperature group by 0.5 °C toward both the low- and high-temperature sides.

To reduce short-term sampling variability and avoid non-physical jumps between adjacent parameter windows, ecological parameters fitted from 11 d subsets were smoothed with an 11 d moving average, following the urban green-space flux-partitioning approach of Soininen et al. (2025). The smoothed R_c, α, and P_{max} were used to estimate R_{eco} and GPP at continuous half-hourly resolution and for subsequent parameter migration, whereas Q10 and θ were kept fixed over the full period.

We used the saturating structure with temperature stratification as the baseline GPP scheme, and evaluated its CH-side fitting performance in Sect. 3.2.1. The pure saturating structure, the saturating structure with VPD inhibition, and Scheme B were retained as structural sensitivity experiments.

2.5 Footprint-informed ecological parameter migration

CH-to-PY migration was designed as footprint- and vegetation-constrained parameter

https://doi.org/10.5194/egusphere-2026-3381
Preprint. Discussion started: 28 July 2026

358 migration, not as a mechanical transfer of CH observed fluxes to PY. The CH-fitted
359 parameters are interpreted as a regional ecological-response reference under weak
360 anthropogenic disturbance, while PY biogenic fluxes are driven by PY-specific
361 temperature, radiation, VPD, and footprint-weighted EVI. This treatment follows the
362 view that EC light-response parameters are apparent ecosystem- or canopy-scale
363 quantities whose magnitudes depend on canopy structure, vegetation amount,
364 phenology, and environmental conditions (Sellers, 1985; Myneni and Williams, 1994;
365 Huete et al., 2002). It is also consistent with light-use-efficiency and satellite-driven
366 GPP models that estimate photosynthetic uptake using vegetation indices and
367 environmental scalars (Monteith, 1972; Running et al., 2004; Xiao et al., 2004;
368 Mahadevan et al., 2008).

369 For GPP-related parameters, EVI_{fp} provides a direct constraint on
370 photosynthetically active vegetation amount and canopy activity. For R_{eco}, EVI_{fp} has a
371 different role: it acts as a footprint-scale vegetation/pervious-surface mask and a
372 capacity-normalization factor for vegetation-associated respiration. Impervious
373 surfaces within the footprint are therefore not assumed to contribute the same
374 respiratory capacity as vegetated surfaces. Under the shared regional climate and
375 broadly similar evergreen broadleaf vegetation background of CH and PY, the CH-
376 derived respiration capacity per unit EVI_{fp} is used as a first-order reference for patchy
377 urban green spaces at PY. This does not imply that soil moisture, substrate supply,
378 irrigation, management intensity, or urban heat-island effects are fully captured by EVI;
379 these factors are treated as part of the structural boundary of the donor–target migration
380 framework and are considered when interpreting the sensitivity results.

381 Because the EC source area changes at half-hourly scales with wind direction,
382 stability, and turbulence conditions, land-cover fractions or vegetation indices within a
383 fixed buffer cannot represent the actual contributing source area of each flux
384 observation. We therefore calculated two-dimensional flux-footprint weights for each
385 time step and used these weights to construct footprint-weighted land-cover fractions
386 (LD_{fp}) and footprint-weighted EVI (EVI_{fp}) following the procedure described in Sect.
387 S5. Land-cover data were taken from the global 10 m GLC_FCS10 product (Zhang et

https://doi.org/10.5194/egusphere-2026-3381
Preprint. Discussion started: 28 July 2026

al., 2025). EVI was obtained from the Harmonized Landsat Sentinel-2 (HLS) vegetation-index products, with 30 m spatial resolution and a revisit cycle of approximately 2–3 d (Neigh, 2021; Neigh, 2025). Compared with the Normalized Difference Vegetation Index (NDVI), EVI is less prone to saturation in high-biomass areas and is more stably related to canopy greenness, the fraction of absorbed photosynthetically active radiation (fAPAR), and seasonal GPP dynamics (Huete et al., 2002; Xiao et al., 2004).

Operationally, we treated the CH temperature-stratified ecological response as the reference function and allowed amplitude-type parameters to vary with vegetation amount and activity in the target footprint. The scaling was applied to ecological capacity parameters rather than to observed fluxes; therefore, migrated PY GPP and R_{eco} were calculated using PY-specific radiation, temperature, VPD, and dynamic EVI_{fp}. Capacity-type parameters fitted at CH within temperature group g, including α, P_{max}, and R_c, were therefore normalized by CH EVI_{fp}:

$$p_{norm,CH}(g) = \frac{P_{CH}(g)}{EVI_{fp,CH}(g)} \quad (10)$$

Here g denotes the temperature group (low, mid, or high), $P_{CH}(g)$ is the ecological parameter fitted at CH within temperature group g, and $P_{norm,CH}(g)$ is the parameter normalized by CH EVI_{fp}. The median $P_{norm,CH}(g)$ within each temperature group was then used as the CH-to-PY parameter-migration coefficient to reduce the influence of anomalous fitting windows or extreme parameter values:

$$C_{norm,CH}(g) = median\left[p_{norm,CH}(g)\right] \quad (11)$$

$C_{norm,CH}(g)$ is the CH-to-PY parameter-migration coefficient for temperature group g. The corresponding PY EVI_{fp} was then used to reconstruct ecological parameters at PY:

$$P_{PY}(t) = C_{norm,CH}\left(g(t)\right) \times EVI_{fp,PY}(t) \quad (12)$$

Here $P_{PY}(t)$ is the migrated ecological parameter at PY for time t. For non-amplitude parameters that are not suitable for EVI proportional scaling, the representative CH statistic within the same temperature group was used. This treatment

https://doi.org/10.5194/egusphere-2026-3381
Preprint. Discussion started: 28 July 2026

preserves the response structure of CH parameters to thermal state while allowing parameter magnitudes to adjust with vegetation activity within the actual PY footprint. Time-step-resolved LD_{fp}, EVI_{fp}, and EVI_{fp}-based migrated parameters together provide the source-area constraint for CH-to-PY parameter migration.

2.6 Sensitivity-based uncertainty assessment

To test the robustness of PY F_{ff} to parameter propagation, processing choices, and ecological model structure, we constructed a targeted sensitivity-based uncertainty framework. This framework was not intended to provide a complete probability distribution for all error sources, nor were the scenarios treated as equally probable samples. Instead, controlled perturbations were applied to processing steps with clear physical meaning to identify the dominant sources of F_{ff} uncertainty.

Uncertainty propagation included two levels. The first level was CH-side ecological-parameter bootstrapping: for each CH scenario, respiration and light-response parameters were resampled 2000 times and migrated to PY using EVI_{fp}, yielding q05, q50, and q95 estimates of R_{eco}, GPP, and F_{ff}. The second level was scenario sensitivity: single-factor or structural-alternative scenarios were constructed for the u* threshold, storage flux, EVI time window, GPP model structure, temperature grouping, daytime-respiration inhibition, CH-side shortwave-radiation input, and human-respiration emissions, and were compared with the baseline scheme.

The final propagation ensemble contained 14 CH-side scenarios and 3 human-respiration scenarios, forming 42 propagation combinations (Sect. S6). CH0 is the baseline scheme. The CH-side scenarios evaluate input and processing sensitivity, ecological model-structure choices, parameter-migration settings, and CH-side shortwave-radiation representativeness. Human-respiration emissions were represented by base, low50, and high50 scenarios, with low50 and high50 equal to 0.5 and 1.5 times the baseline human-respiration emission, respectively.

For any CH scenario s, human-respiration scenario r, bootstrap member b, and time t, F_{ff} was propagated as:

$$F_{ff}(b,s,r,t) = F_{cr}(s,t) - R_{eco}(b,s,t) + GPP(b,s,t) - F_{hu}(r,t) \quad (13)$$

https://doi.org/10.5194/egusphere-2026-3381
Preprint. Discussion started: 28 July 2026

Here F_{ff} (b, s, r, t) is the propagated F_{ff} estimate for the corresponding scenario and bootstrap member; F_{cr} (s, t) is the storage-corrected net CO_2 flux at PY under scenario s; R_{eco} (b, s, t) is ecosystem respiration driven by migrated parameters; GPP (b, s, t) is gross primary productivity driven by migrated parameters; and F_{hu} (r, t) is the human-respiration CO_2 flux.

The central estimate at each time was the bootstrap median, and the parameter-propagation range was represented by q05–q95. Scenario uncertainty was evaluated as the difference from the baseline CH0 + human base configuration:

$$\Delta F_{ff}(s,t) = F_{ff}(s,base,t) - F_{ff}(CH0,base,t) \quad (14)$$

Here F_{ff} (s, base, t) denotes the bootstrap-median F_{ff} under CH scenario s and the base human-respiration setting. ΔF_{ff} (s, t) denotes the F_{ff} offset for scenario s relative to baseline CH0 at time t. Positive values indicate that the scenario increases F_{ff}, whereas negative values indicate that it decreases F_{ff}. ΔF_{ff} was then summarized at overall, hourly, and monthly scales to diagnose how different uncertainty sources affect the mean, diurnal variation, and seasonal variation of F_{ff}.

3 Results and discussion

3.1 Net CO_2 flux variability and source-area controls

3.1.1 Diurnal and seasonal patterns of net CO_2 flux

Hourly storage-corrected CO_2 fluxes (F_{cr}) during 2023–2024 showed a clear urban–suburban contrast (Fig. 2a–b). Overall, the mean F_{cr} at PY was 2.04 μmol m^{-2} s^{-1}, indicating a year-round net CO_2 source, whereas the mean F_{cr} at CH was −2.57 μmol m^{-2} s^{-1}, indicating a year-round net CO_2 sink. Urban EC studies generally show that urban surfaces are net CO_2 sources, with anthropogenic emissions, especially traffic, building-energy use, and residential activities, providing important contributions to urban CO_2 fluxes. By contrast, suburban or highly vegetated areas are more likely to show pronounced biogenic uptake signals (Crawford et al., 2011; Järvi et al., 2012). The annual mean difference between PY and CH therefore reflects the control exerted by source-area urbanization and vegetation cover on net CO_2 exchange.

https://doi.org/10.5194/egusphere-2026-3381
Preprint. Discussion started: 28 July 2026

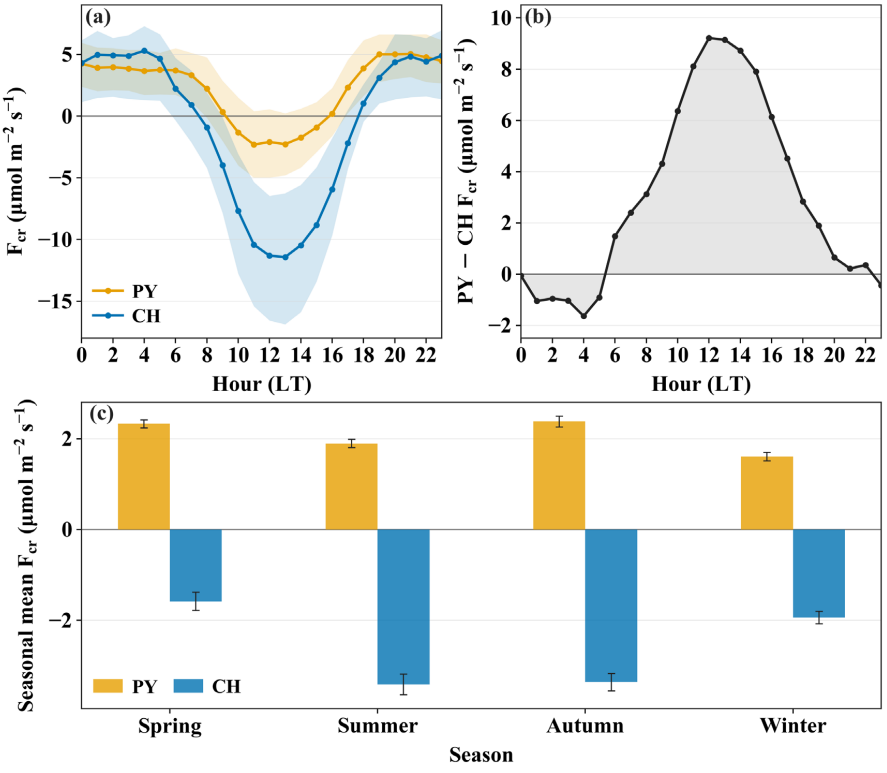

Figure 2. Diurnal and seasonal characteristics of corrected CO_2 flux (F_{cr}) at the PY and CH sites. **(a)** Mean diurnal F_{cr} at PY and CH; shading indicates the interquartile range (Q25–Q75). **(b)** Mean diurnal PY–CH contrast in F_{cr}. **(c)** Seasonal mean F_{cr} at PY and CH for spring (March–May), summer (June–August), autumn (September–November), and winter (December–February), with error bars indicating the standard error. Positive values indicate net CO_2 release to the atmosphere, whereas negative values indicate net uptake.

At the diurnal scale, both sites showed higher nighttime and lower daytime fluxes, but with very different amplitudes. At CH, F_{cr} was mostly positive at night, became rapidly negative as radiation increased during the day, and reached the strongest uptake around 12:00–13:00, with a mean of about −11 μmol m^{-2} s^{-1}. At PY, daytime F_{cr} also decreased, but only approached weakly negative or near-neutral values around midday. This suggests that vegetation uptake was still detectable at PY, but its expression in the net flux was partly masked by persistent urban anthropogenic emissions. Similar behavior has been reported for a tropical residential neighborhood in Singapore and other urban EC studies: urban vegetation can absorb part of the daytime CO_2, but it

https://doi.org/10.5194/egusphere-2026-3381
Preprint. Discussion started: 28 July 2026

usually does not fully offset anthropogenic emissions, so urban sites generally remain net sources (Velasco et al., 2013; Velasco and Roth, 2010).

At the seasonal scale, mean F_{cr} values at PY were 2.33, 1.89, 2.38, and 1.61 μmol m^{-2} s^{-1} in spring, summer, autumn, and winter, respectively (Fig. 2c). PY therefore remained a net CO_2 source throughout the year, although net emissions were lower in summer. At CH, F_{cr} was negative in all seasons, with spring, summer, autumn, and winter means of −1.59, −3.41, −3.36, and −1.94 μmol m^{-2} s^{-1}, respectively. Stronger uptake during the warm growing-season months is consistent with the long summer carbon-sink duration observed in subtropical urban vegetation and the seasonally active photosynthesis of South China subtropical evergreen forests (Zhang et al., 2019; Wang et al., 2023). Multi-year urban and suburban EC observations also show that sites with higher vegetation cover usually exhibit stronger growing-season CO_2 uptake, whereas seasonal variation at urban sites is jointly controlled by anthropogenic emissions and biogenic processes (Järvi et al., 2012; Menzer and McFadden, 2017).

Seasonal diurnal patterns further show that biogenic regulation of net flux is stronger during the growing season (Fig. S1). CH exhibited the largest diurnal amplitude and strongest midday uptake in summer, consistent with high-vegetation sites having both stronger ecosystem respiration and stronger photosynthetic uptake during the growing season. Although PY remained a net CO_2 source throughout the year, its diurnal amplitude in summer and autumn was also higher than in spring and winter, indicating that clear biogenic modulation remains embedded in the net flux of this mixed urban source area. In other words, low daytime F_{cr} and enhanced growing-season amplitude at PY should not be interpreted as weaker anthropogenic emissions, but as the net result of anthropogenic emissions and vegetation uptake acting together.

3.1.2 Footprint land cover and sectoral controls

Because urban EC source areas vary with wind direction, turbulence state, and boundary-layer conditions, footprint modelling combined with high-resolution land-cover data is needed to interpret spatial heterogeneity in urban CO_2 fluxes (Crawford and Christen, 2015; Kljun et al., 2015).

https://doi.org/10.5194/egusphere-2026-3381
Preprint. Discussion started: 28 July 2026

Wind-sector analysis showed that F_{cr} at PY had clear source-area dependence (Fig. 3). High F_{cr} mainly occurred in the NE, N, and NW sectors, with mean values of about 3.59, 2.83, and 2.52 μmol m^{-2} s^{-1}, respectively, clearly higher than those in the W and SW sectors. Correspondingly, impervious fractions were relatively high in the N and NW sectors, about 33 % and 37 %, respectively. Although the NE impervious fraction was slightly lower than those in the N and NW sectors, the NE sector still contained a strong mixture of urban hard surfaces and forest patches. Correlations across the eight wind-sector means showed that sector-mean F_{cr} at PY was strongly positively correlated with impervious fraction ($r = 0.77$). F_{cr} was also positively correlated with forest fraction ($r = 0.52$), while impervious and forest fractions were themselves positively correlated ($r = 0.61$). This result indicates that the positive forest–F_{cr} correlation at PY should not be interpreted as forest cover increasing CO_2 emissions. It more likely reflects collinearity caused by the spatial coexistence of campus forests, roads, buildings, and hard surfaces in and around the PY university-town area. In other words, forest patches at PY are not independent biogenic source areas; they are often embedded within urbanized source areas and therefore carry part of the urban-activity source-area signal at the sector scale.

By contrast, the directional pattern at CH was more consistent with biogenic control. F_{cr} was mostly negative across CH sectors, with the strongest net uptake in the W, SW, and S sectors, where mean F_{cr} values were about −7.44, −6.74, and −6.76 μmol m^{-2} s^{-1}, respectively; these sectors generally had higher forest fractions. Sector-scale correlations showed a negative relationship between F_{cr} and forest fraction at CH ($r = -0.76$), indicating that source areas with higher forest cover generally corresponded to stronger net CO_2 uptake. The comparison between CH and PY therefore demonstrates that the influence of land cover on F_{cr} is site dependent. At CH, forest cover is closer to a true biogenic control. At PY, forest, impervious surface, and human-activity source areas are tightly coupled, so correlation and causality must be separated carefully. Similarly, Pérez-Ruiz et al. (2020) showed that different urban land-cover types influence the response of CO_2 fluxes to environmental drivers, highlighting land-cover heterogeneity as an important factor in explaining flux differences within cities.

https://doi.org/10.5194/egusphere-2026-3381
Preprint. Discussion started: 28 July 2026

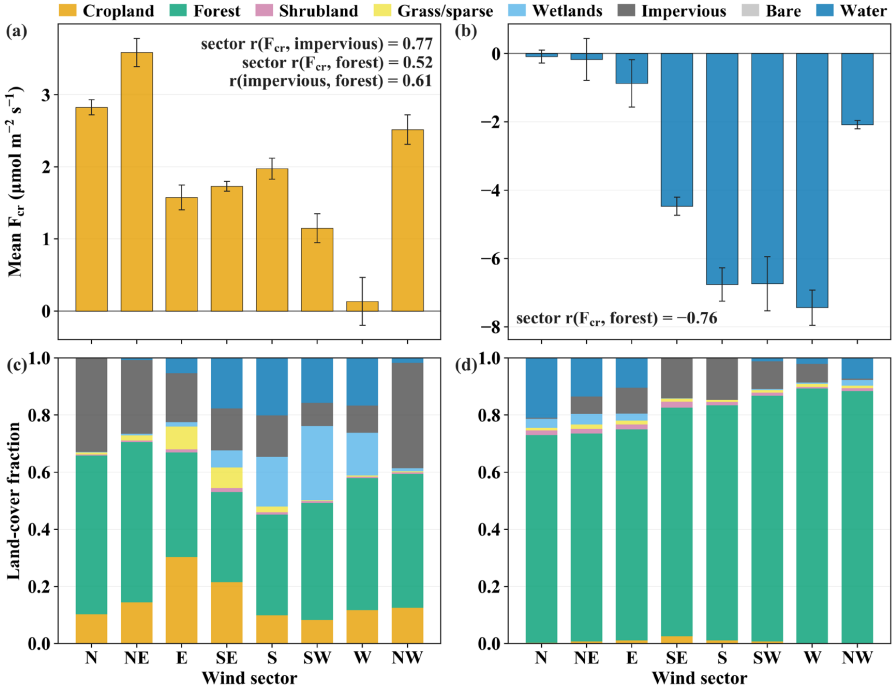

Figure 3. Directional variation in corrected CO_2 flux (F_{cr}) and footprint-weighted land-cover composition at the PY and CH sites. Panels **(a)** and **(b)** show sectoral mean F_{cr} at PY and CH, respectively; error bars indicate the standard error across hourly values. Panels **(c)** and **(d)** show the corresponding footprint-weighted land-cover fractions for PY and CH, respectively. The eight sectors were defined as 45° wind-direction bins centered on the cardinal and intercardinal directions, with N spanning 337.5°–360° and 0°–22.5°; land-cover fractions were calculated by averaging the footprint-weighted land-cover composition of all valid records within each sector.

Sector-hour heat maps and hourly correlation analyses further support this interpretation (Figs. S2 and S3). High F_{cr} at PY was concentrated not only in more urbanized directions such as N, NE, and NW, but also during nighttime, evening, and morning-rush periods, indicating that its diurnal variation was jointly regulated by wind-sector source area, local activity, and biogenic uptake. Hourly correlations also showed a positive relationship between F_{cr} and impervious fraction at PY, suggesting that hard surfaces and built-up source areas are important indicators of higher net CO_2 emissions. F_{cr} at PY was also positively correlated with forest fraction, but this likely reflects the co-occurrence of urban green space with roads and buildings, given their sectoral collinearity with impervious surfaces (Fig. 3). At CH, most sectors became

https://doi.org/10.5194/egusphere-2026-3381
Preprint. Discussion started: 28 July 2026

clearly negative during the day, and F_{cr} was negatively correlated with forest fraction, more closely reflecting biogenic uptake control in a highly vegetated source area. Beyond land cover, F_{cr} at both sites was significantly negatively correlated with shortwave radiation, showing that enhanced daytime radiation and vegetation photosynthesis were important drivers of lower net CO_2 flux. Correlations of F_{cr} with temperature, VPD, relative humidity, and wind speed more likely reflect the combined effects of diurnal phase, turbulent mixing, and biogenic processes, and should not be interpreted as independent causal effects of single variables.

Overall, source-area analysis shows that F_{cr} at PY is jointly shaped by mixed urban land cover, especially the co-occurrence of impervious surfaces and campus green space, together with wind-sector source areas and environmental conditions, whereas F_{cr} at CH mainly reflects biogenic uptake control by high forest cover. F_{cr} can therefore reveal the spatiotemporal heterogeneity of urban net CO_2 exchange, but it cannot directly represent anthropogenic CO_2 flux. For mixed urban source areas such as PY, where green space and built-up land are highly interwoven, R_{eco}, GPP, and human respiration must be removed before anthropogenic CO_2 flux can be more robustly extracted.

3.2 Footprint-informed ecological parameterization

3.2.1 Donor-site respiration and GPP light-response fitting

Having established CH as a highly vegetated and weakly disturbed donor site, we next evaluated whether its respiration and GPP light-response parameters could provide a stable ecological reference for parameter migration. This step tests whether the donor-site fitting produced physiologically interpretable parameters and whether the selected GPP structure adequately captured CH-side photosynthetic variability.

In the baseline scheme, nighttime ecosystem respiration was represented using a fixed Q10 value of 1.64. Seasonal variation was therefore expressed mainly through the fitted base respiration coefficient R_c, rather than Q10 itself. Nighttime respiration fitting at CH showed acceptable agreement between observations and simulations, with R = 0.608, RMSE = 1.419 μmol m^{-2} s^{-1}, and bias = −0.004 μmol m^{-2} s^{-1} (Fig. S4a). Thus,

https://doi.org/10.5194/egusphere-2026-3381
Preprint. Discussion started: 28 July 2026

under the present data-screening and parameterization framework, the nighttime respiration model showed no obvious systematic overestimation or underestimation and provided a basis for subsequent daytime respiration extrapolation and parameter migration.

CH-side GPP light-response fitting further showed that the temperature-stratified scheme captured photosynthetic variation reasonably well. The baseline GPP fit had R = 0.659, RMSE = 4.904 μmol m^{-2} s^{-1}, and MAE = 3.679 μmol m^{-2} s^{-1}, outperforming the pure saturating structure and the saturating structure with VPD inhibition (Fig. S4b–d). The ecological parameters in the CH baseline scheme were not constant; they varied over time and among temperature groups (Fig. S5). R_c fluctuated during the year, with monthly medians of about 0.96–1.36. Among the GPP light-response parameters, α and P_{max} also varied with time and thermal state, with monthly medians of about 0.026–0.052 and 16.8–43.8 μmol m^{-2} s^{-1}, respectively. These results indicate interpretable ecological variability in CH respiration and light-response parameters, rather than dominance by random fitting error. θ was treated as a fixed shape parameter in the baseline scheme, with a value of 0.2, and is therefore not interpreted as an independent seasonal parameter.

Comparison among GPP structural schemes further supports the temperature-stratified structure as the baseline. Compared with the pure saturating structure and the saturating structure with VPD inhibition, the temperature-stratified scheme had a higher R and lower RMSE and MAE, indicating that it better captured hourly variation in the CH GPP target. In the saturating + VPD inhibition structure, the fitted k_{VPD} was close to zero. This suggests that, under the humid subtropical background and screened samples used here, the explicit VPD inhibition term did not provide additional explanatory power beyond the temperature-stratified structure. This result does not deny the physiological relevance of VPD; rather, it indicates that differences in thermal state better explained light-response variation in this dataset. We therefore selected the temperature-stratified structure as the baseline and used the pure saturating and saturating + VPD inhibition structures as structural sensitivity scenarios in the uncertainty analysis.

https://doi.org/10.5194/egusphere-2026-3381
Preprint. Discussion started: 28 July 2026

3.2.2 EVI_{fp}-constrained parameter migration to the urban target

We evaluated whether the donor–target design met the ecological comparability conditions required for EVI_{fp}-constrained parameter migration. This evaluation focused on three aspects: whether CH could provide a relatively clean ecological-response reference, whether CH and PY shared a comparable regional environmental and phenological background, and whether vegetation amount and activity in the PY footprint could be represented by dynamic EVI_{fp}. The footprint land-cover contrast shown in Fig. 3c–d and Table S3 supports CH as a vegetation-dominated donor and PY as a heterogeneous urban target, indicating that PY cannot directly use CH observed fluxes or unscaled CH parameters.

Environmental and vegetation diagnostics further support this constrained-migration design. Figure S6 shows that CH and PY have highly consistent seasonal phases in air temperature and daytime shortwave radiation. VPD has a similar seasonal magnitude at the two sites, but its month-to-month consistency is relatively weak, indicating shared regional seasonal forcing but non-identical microclimatic conditions. This microclimatic difference does not invalidate the migration framework because CH meteorological time series were not imposed on PY. Instead, the migrated PY biogenic fluxes were driven by PY-specific temperature, radiation, and VPD, while CH provided the vegetation-normalized ecological-response reference. Table S3 also shows broadly similar urban-forest types at the two sites, whereas vegetation cover and anthropogenic influence differ substantially. Consistently, Fig. 4 shows that EVI_{fp} is overall higher at CH than at PY, as expected from the higher vegetation cover at CH. Although EVI_{fp} at PY is lower, it retains a clear seasonal pattern, with higher values in summer and lower values in winter and spring. This recognizable phenological signal supports the use of EVI_{fp} for scaling ecological capacity in the dynamic PY footprint. For R_{eco}, EVI_{fp} should be interpreted as scaling vegetation-associated respiratory capacity within the dynamic footprint, rather than assuming that all urban surfaces or soil processes respond linearly to canopy greenness. Thus, the similar seasonal phases in temperature and radiation support CH as a same-region donor, whereas PY's warmer background and

https://doi.org/10.5194/egusphere-2026-3381
Preprint. Discussion started: 28 July 2026

weaker VPD consistency define the extrapolation boundary.

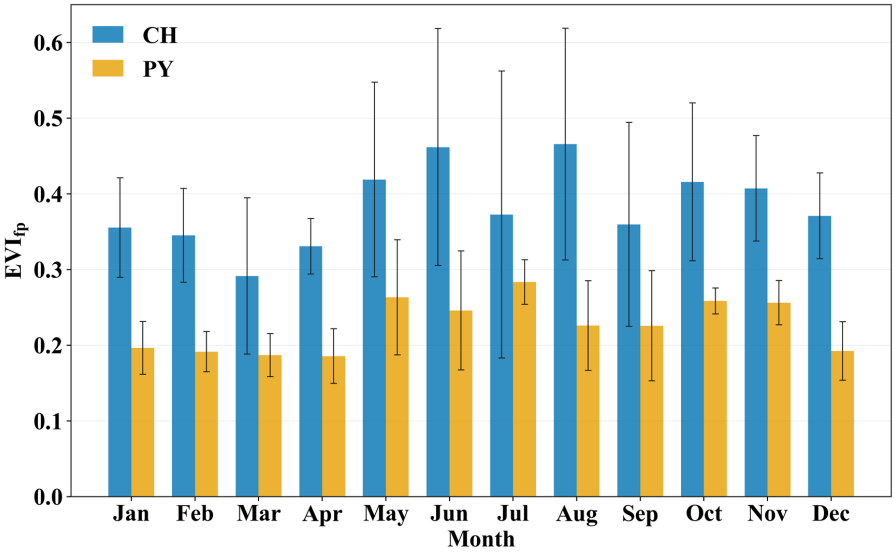

Figure 4. Monthly variation of footprint-weighted vegetation activity at the CH and PY sites. Bars show the monthly mean footprint-weighted enhanced vegetation index (EVI_{fp}) for CH and PY, and error bars indicate ±1 standard deviation.

The migrated PY ecological-parameter ranges are consistent with these diagnostics. Under the baseline scheme, the 5 %–95 % range of α at PY was 0.007–0.029, the 5 %–95 % range of P_{max} was 5.30–13.89 μmol m^{-2} s^{-1}, and the 5 %–95 % range of R_c was 0.351–0.762. Compared with the CH donor site, the capacity-type parameters at PY were substantially reduced but did not approach zero, consistent with the presence of urban green space in the PY footprint and with lower vegetation cover and activity than at CH. All migrated parameters were non-negative. Migrated GPP showed a typical daytime increase and approached zero at night, whereas R_{eco} remained positive throughout the day and varied more smoothly (Fig. 5). Recent urban flux-partitioning work provides the closest benchmark for the migrated PY biogenic fluxes. Soininen et al. (2025) reported median GPP peaks of about 8.8–11.9 μmol m^{-2} s^{-1} for a street-sector footprint with substantial vegetation cover, together with a mean ecosystem respiration of about 3.9 μmol m^{-2} s^{-1}. The migrated PY maximum GPP of 10.83 μmol m^{-2} s^{-1} is therefore comparable to this urban mixed-source GPP benchmark. For R_{eco}, additional magnitude support comes from urban and subtropical vegetated

https://doi.org/10.5194/egusphere-2026-3381
Preprint. Discussion started: 28 July 2026

surfaces. Soil respiration ranged from 2.6 to 6.7 μmol m^{-2} s^{-1} across vegetated and managed cover types in greater Boston (Decina et al., 2016), and annual mean soil respiration in Hefei park and campus green spaces was 2.51–2.64 μmol m^{-2} s^{-1} (Tao et al., 2016). Eddy-covariance flux partitioning in a subtropical Chinese urban forest reported mean R_{eco} of about 3.0 μmol m^{-2} s^{-1}, with condition-specific means ranging from 1.9 to 4.0 μmol m^{-2} s^{-1} under heatwave and drought conditions (Yang et al., 2025). Humid subtropical forests in South China also show comparable total soil-respiration magnitudes of about 2.7–3.0 μmol m^{-2} s^{-1} after unit conversion (Yi et al., 2007). The migrated PY maximum R_{eco} of 4.54 μmol m^{-2} s^{-1} therefore falls within a plausible range for vegetated and managed pervious surfaces. This comparison is a magnitude-consistency check rather than direct validation, but it supports the view that the EVI_{fp} constraint did not generate unrealistically large biogenic fluxes. Nevertheless, R_{eco} remains more indirectly constrained by EVI_{fp} than GPP.

Taken together, Fig. 3c–d, Fig. 4, Table S3, and Fig. S6 support the ecological consistency of the CH-to-PY migration design: CH provides a cleaner ecological-response reference under a shared regional background, while PY requires EVI_{fp}-based scaling because of its lower vegetation activity and stronger source-area heterogeneity. The migration hypothesis is supported by three lines of evidence: comparable regional climatic and phenological forcing, EVI_{fp}-based separation of vegetation-associated source areas from impervious surfaces, and migrated GPP and R_{eco} magnitudes that fall within reported urban green-space and mixed-source ranges. Direct independent validation of donor-site parameter migration remains limited, so this approach is treated as an ecologically constrained parameterization rather than a universally validated empirical law. Its influence on F_{ff} is further evaluated through the sensitivity analyses in Sect. 3.5.

3.3 Partitioned flux dynamics at the urban target site

3.3.1 Diurnal partitioning of CO_2 flux components

Using the biogenic components constrained above, we partitioned the corrected CO_2 flux (F_{cr}) at PY and examined the resulting anthropogenic CO_2 flux (F_{ff}). This step links

https://doi.org/10.5194/egusphere-2026-3381
Preprint. Discussion started: 28 July 2026

the ecological correction to the question of how biogenic uptake and anthropogenic emissions jointly shape net exchange in a mixed urban footprint.

Figure 5 shows that F_{cr} at PY has typical characteristics of a mixed urban green-space source area. It is positive at night and in the evening, decreases substantially during the day as GPP increases, and becomes negative around midday. Correspondingly, GPP reaches high values during 11:00–14:00, with an hourly mean peak of about 6.44 μmol m^{-2} s^{-1}. R_{eco} shows a smaller diurnal amplitude and remains around 1.14–1.45 μmol m^{-2} s^{-1}. These results show that, although PY is an urban site, its net flux still contains a pronounced biogenic uptake signal. In other words, negative daytime F_{cr} does not mean that anthropogenic CO_2 emissions disappear; it means that biogenic uptake offsets part of the anthropogenic emissions at the net-exchange level.

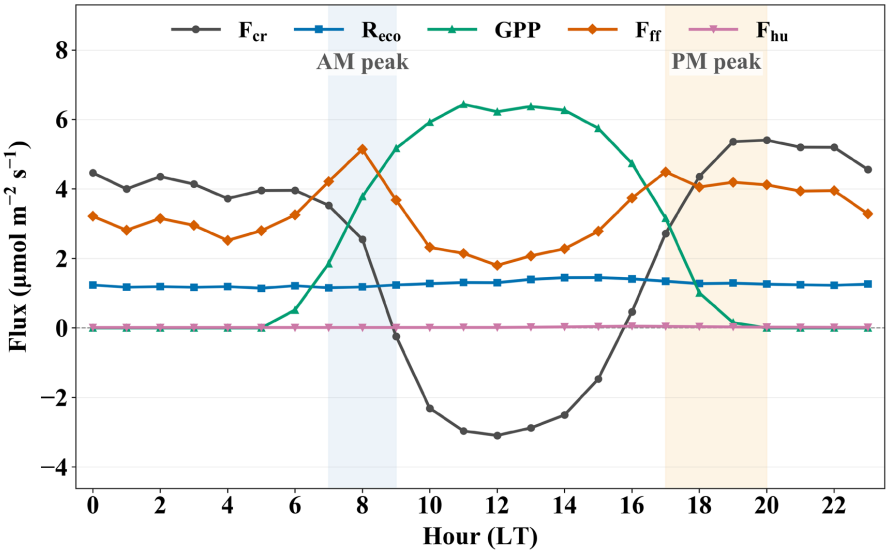

Figure 5. Main-case diurnal decomposition of corrected CO_2 flux at the PY site. Lines show hourly means of corrected flux (F_{cr}), ecosystem respiration (R_{eco}), gross primary productivity (GPP), anthropogenic CO_2 flux (F_{ff}), and human respiration flux (F_{hu}). Shaded intervals mark the morning (07:00–09:00 LT) and evening (17:00–20:00 LT) peak windows in local time.

After partitioning, F_{ff} remained positive throughout the day, with hourly means of about 1.80–5.14 μmol m^{-2} s^{-1} and a 24 h mean of about 3.29 μmol m^{-2} s^{-1}. Its diurnal variation showed a clear anthropogenic-activity rhythm: the 07:00–09:00 morning-rush mean was about 4.34 μmol m^{-2} s^{-1}, with the daily maximum at 08:00; the 17:00–20:00

https://doi.org/10.5194/egusphere-2026-3381
Preprint. Discussion started: 28 July 2026

evening-rush mean was about 4.22 μmol m^{-2} s^{-1}; and the 11:00–14:00 midday mean decreased to about 2.08 μmol m^{-2} s^{-1}. This double-peak structure is consistent with the rhythms of commuting, campus travel, campus services, and surrounding road traffic in the Guangzhou Higher Education Mega Center, and with urban EC source-partitioning studies showing that fossil-fuel or anthropogenic CO_2 fluxes often exhibit traffic- or activity-related peaks (Lee et al., 2021; Wu et al., 2022).

In magnitude, F_{ff} at PY lies between two relevant urban green-space references. Yang et al. (2025) reported a low-intensity traffic-emission background of 0–1.93 μmol m^{-2} s^{-1} for a campus urban-forest environment in Nanjing, which is closer to a green-space setting than to a dense traffic corridor. In contrast, Soininen et al. (2025) studied a Helsinki footprint influenced by both urban green space and a busy street sector, where light-response-curve partitioning inferred anthropogenic CO_2 fluxes of 3.1–10.9 μmol m^{-2} s^{-1}. The PY F_{ff} range of 1.80–5.14 μmol m^{-2} s^{-1} falls between these two references, consistent with the source-area character of the Guangzhou Higher Education Mega Center, where green space, roads, buildings, and water bodies are interwoven.

These results show how biogenic and anthropogenic components jointly shape the observed net exchange at PY. During midday, strong GPP offsets a substantial part of the anthropogenic source and can drive F_{cr} close to zero or negative values. During the morning and evening periods, weaker biogenic uptake and enhanced anthropogenic activity allow F_{ff} to dominate the net-flux signal. Thus, the urban net CO_2 flux is not controlled by a single source process, but by the changing balance between persistent anthropogenic emissions and temporally variable biogenic uptake.

3.3.2 Monthly variation in F_{ff} and its potential drivers

At the monthly scale, F_{ff} at PY remained positive in all months, indicating a persistent anthropogenic CO_2 source signal within the PY footprint. Figure 6a shows that monthly median F_{ff} was about 2.59–4.29 μmol m^{-2} s^{-1}, with lower values in August and higher values in October–November. The lowest monthly median occurred in August, about 2.59 μmol m^{-2} s^{-1}, while October and November increased to about 3.94 and 4.29 μmol

https://doi.org/10.5194/egusphere-2026-3381
Preprint. Discussion started: 28 July 2026

752 m^{-2} s^{-1}, respectively. This range indicates moderate month-to-month variability
753 superimposed on a persistent anthropogenic source signal.

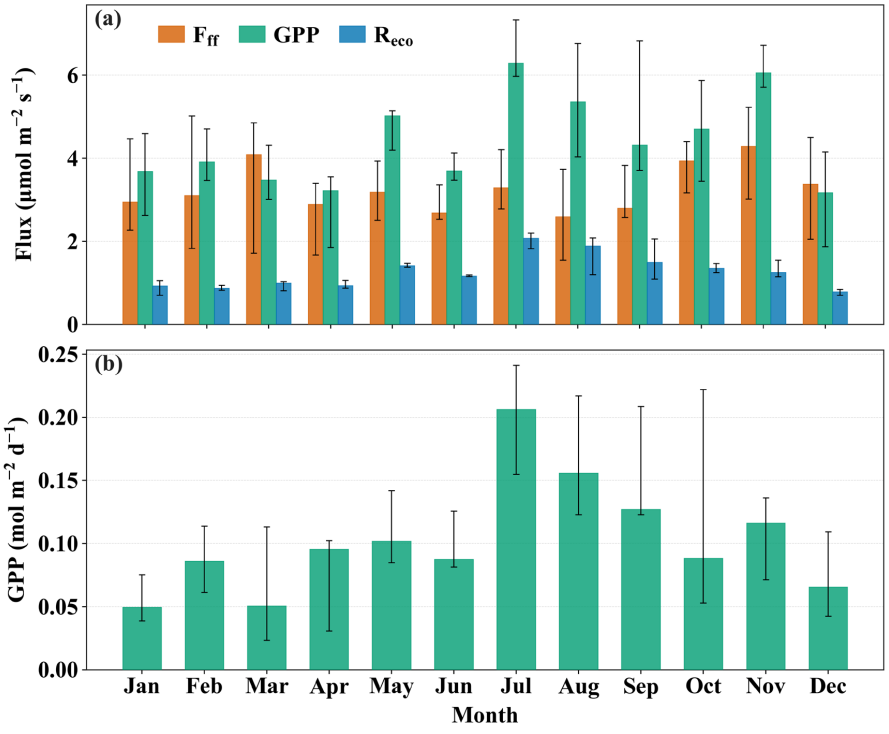

754
755 **Figure 6.** Monthly variations in daily aggregated partitioned CO_2 fluxes and daytime
756 cumulative GPP at the PY site. **(a)** Monthly medians of daily aggregated anthropogenic CO_2
757 flux (F_{ff}), daytime mean GPP, and ecosystem respiration (R_{eco}), with error bars showing the
758 interquartile range (Q25–Q75) derived from daily values within each month. **(b)** Monthly
759 medians of daily daytime cumulative GPP (mol m^{-2} d^{-1}), also shown with interquartile ranges.

760 This monthly pattern should not be attributed to a single factor. PY is located in a
761 university-town area, where summer and winter vacations, the start of semester, campus
762 services, and surrounding road traffic can influence local anthropogenic emissions.
763 August falls within the summer vacation, when teaching, commuting, and internal
764 campus service activities are reduced; this may help explain the low F_{ff} values. In
765 October–November, regular teaching activities and surrounding road activity resume,
766 providing a reasonable anthropogenic-activity background for higher F_{ff}. However, the
767 PY EC footprint does not cover only the campus interior; it also includes roads,
768 residential areas, water bodies, and urban service sources. Vacation effects may

https://doi.org/10.5194/egusphere-2026-3381
Preprint. Discussion started: 28 July 2026

therefore contribute to the monthly variation, but they should be interpreted together with other footprint-scale sources and environmental controls rather than as a single dominant driver of F_{ff}.

Meteorological and ecological conditions also modulate month-to-month F_{ff} variation. Precipitation was notably high in August, which may have further reduced F_{ff} by reducing travel, changing road-operating conditions, or altering activity intensity within the effective footprint. At the same time, vegetation activity and GPP remained strong in August, and ecological correction and changes in source-area vegetation weight may also have affected the monthly median F_{ff} (Figs. 4 and S7). In contrast, precipitation decreased substantially in October–November, and the combination of resumed campus activity and less rainfall is consistent with stronger anthropogenic sources. Monthly variation in PY F_{ff} should therefore be interpreted as the combined result of anthropogenic activity, meteorological conditions, ecological correction, and dynamic footprints, rather than as a direct response to a single driver.

3.3.3 Eco-meteorological controls on GPP and R_{eco}

Monthly variation in GPP and R_{eco} provides ecological context for understanding why the apparent net CO_2 source strength and the inferred F_{ff} vary differently through the year. Figures 6a–b show that GPP and R_{eco} at PY both strengthened in the warm season and weakened in winter. This is consistent with the basic understanding that GPP in EC flux partitioning is jointly controlled by radiation, vegetation activity, and water status, whereas R_{eco} is mainly regulated by temperature and substrate availability (Reichstein et al., 2005; Lasslop et al., 2010).

For GPP, the daytime cumulative GPP shown in Fig. 6b is more appropriate for explaining seasonality because GPP is intrinsically a daytime process, whereas all-day averages are affected by nighttime zeros, daylength, and the distribution of valid samples. Daytime cumulative GPP at PY peaked in July, with a monthly median of about 0.206 mol m^{-2} d^{-1}. It remained relatively high in August–September but did not continue to increase, and it decreased clearly in winter. High PAR, temperature, and EVI_{fp} in July jointly supported strong photosynthesis. In August–September, heavy

https://doi.org/10.5194/egusphere-2026-3381
Preprint. Discussion started: 28 July 2026

rainfall and cloudy conditions may have reduced effective radiation, while elevated VPD during some periods may also have induced stomatal regulation and limited further GPP enhancement (Fig. S7). The Nanjing campus urban-forest study of Yang et al. (2025) also showed that urban-forest GPP and R_{eco} are sensitive to radiation, temperature, and water status. Thus, warm-season enhancement of PY GPP and its fluctuations in rainy months are reasonable and should not be interpreted as a monotonic response to temperature or precipitation alone.

Monthly variation in R_{eco} more directly reflects temperature control. Monthly median R_{eco} at PY was about 0.79–2.07 μmol m^{-2} s^{-1}, higher in summer and early autumn and lower in winter, consistent with a Q10-type respiration model and seasonal temperature variation. It is important to note that R_{eco} in this study was not fitted directly at PY. It was obtained by migrating CH-side respiration parameters with EVI_{fp} constraints and driving them with PY temperature. Its warm-season enhancement and winter reduction therefore indicate that the migrated ecological respiration component has reasonable physiological meaning.

Overall, the monthly biogenic components at PY show clear eco-meteorological consistency: GPP increases with stronger radiation and greater vegetation activity under warm-season conditions, but is modulated by rainfall, cloudiness, and VPD, whereas R_{eco} mainly follows seasonal temperature variation. This supports the physiological plausibility of the migrated biogenic components. More importantly for flux interpretation, warm-season vegetation activity can reduce the apparent net CO_2 source strength even when F_{ff} remains positive, whereas weaker winter biogenic uptake allows the anthropogenic component to be more directly expressed in F_{cr}.

3.4 Independent evidence for the anthropogenic interpretation of F_{ff}

Sections 3.1–3.3 show that PY F_{ff} remained positive throughout the day and year and exhibited a clear morning peak and weaker evening peak. Because F_{ff} is inferred after ecological correction, its anthropogenic attribution requires independent evaluation. We therefore evaluate F_{ff} using three complementary lines of evidence: pollutant diurnal patterns, wind-sector land cover and traffic activity, and footprint-weighted inventories

https://doi.org/10.5194/egusphere-2026-3381
Preprint. Discussion started: 28 July 2026

that provide magnitude context and insight into possible spatial-allocation mismatch. These comparisons are not used to validate F_{ff} as a direct traffic-emission estimate or to attribute it to a single source category; rather, they provide independent consistency checks for its anthropogenic-emission interpretation (Velasco and Roth, 2010; Crawford and Christen, 2015; Wu et al., 2022).

3.4.1 Consistency with pollutant diurnal patterns

Figure 7 compares the 24 h standardized diurnal patterns of F_{ff} with NO_x, CO, CO_2, and $PM_{2.5}$. Z-score standardization removes differences in units and magnitudes among variables and focuses on phase, peak timing, and relative shape, rather than absolute concentrations or fluxes. Figure 7a shows that F_{ff} has a clear morning peak during 07:00–09:00 and increases again during 17:00–20:00. NO_x and CO also increase synchronously during the morning peak. Shape-correlation results further show that F_{ff} has the highest 24 h standardized-pattern correlation with NO_x, with Pearson r about 0.62; its correlation with CO is the second highest, about 0.53; and its correlations with CO_2 and $PM_{2.5}$ are weaker, about 0.36 and 0.34, respectively (Fig. 7b). This ranking is physically consistent with urban anthropogenic emissions. NO_x is sensitive to motor vehicles and local combustion processes (Parrish, 2006; Juchem et al., 2025), CO is commonly used as an auxiliary tracer for combustion sources (Turnbull et al., 2011), whereas CO_2 concentration and $PM_{2.5}$ are more strongly affected by boundary-layer height, regional transport, secondary formation, and non-traffic sources (Xueref-Remy et al., 2018; Guo et al., 2014). Compared with CO_2 concentration alone, the diurnal consistency of F_{ff} with NO_x and CO therefore provides stronger support for a traffic- or combustion-related anthropogenic CO_2 flux.

Peak-window analysis further strengthens this interpretation. During the morning peak (07:00–09:00) relative to the 04:00–06:00 background, F_{ff} increased by about 52 %, and NO_x increased by about 59 %, with similar amplitudes. CO and $PM_{2.5}$ also showed positive increases, but with smaller amplitudes (Fig. 7c). During the evening peak from 17:00 to 20:00, F_{ff} and NO_x increased by about 44 % and 35 % relative to 14:00–16:00, respectively, whereas CO_2 and $PM_{2.5}$ showed weaker changes (Fig. 7d).

https://doi.org/10.5194/egusphere-2026-3381
Preprint. Discussion started: 28 July 2026

These results indicate that the morning and evening F_{ff} peaks are unlikely to be artifacts of the partitioning procedure; instead, they show an activity rhythm consistent with traffic- and combustion-related pollutants. Similarly, Wu et al. (2022) emphasized that the fossil-fuel component in urban EC CO_2 fluxes should be evaluated using CO, ^{14}C, or high-resolution emission information, rather than inferred from the net CO_2 flux pattern alone.

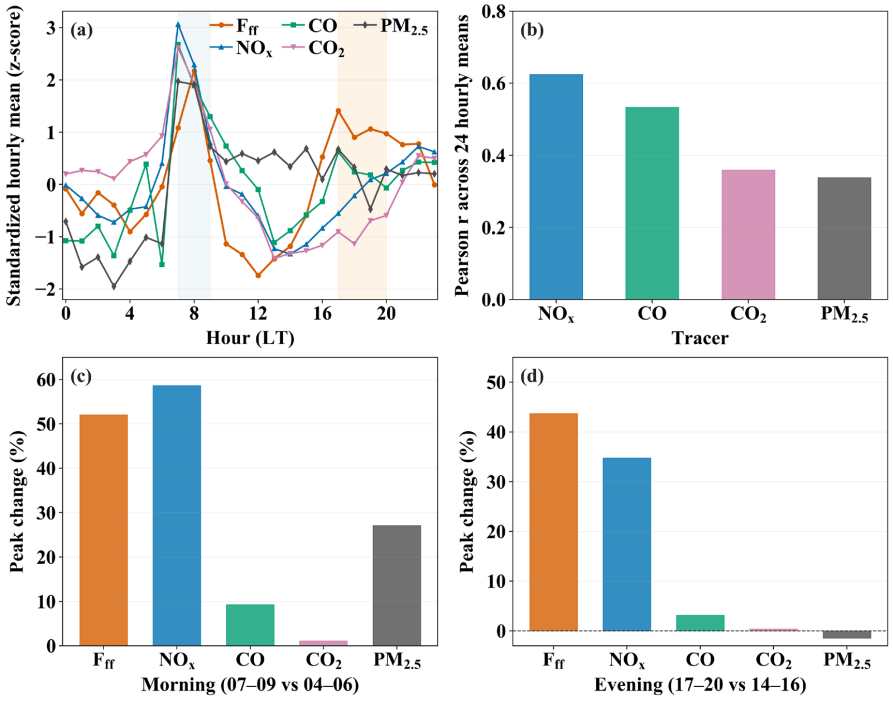

Figure 7. Diurnal-shape consistency and peak-window enhancement characteristics of the anthropogenic CO_2 flux (F_{ff}) and selected atmospheric tracers at the PY site. **(a)** Standardized hourly mean (z-score) curves for F_{ff} and the selected tracers. Each series was first aggregated independently to hourly means and then standardized to highlight shape similarity rather than magnitude. The shaded bands indicate the morning (07:00–09:00 LT) and evening (17:00–20:00 LT) peak period. **(b)** Pearson correlation coefficients between the standardized 24 h shape of F_{ff} and each tracer, computed across the 24 h mean values. **(c)** Morning peak-window enhancement, expressed as the percentage change from the pre-window (04:00–06:00 LT) to the peak window (07:00–09:00 LT). **(d)** Evening peak-window enhancement, expressed as the percentage change from the pre-window (14:00–16:00 LT) to the peak window (17:00–20:00 LT).

3.4.2 Wind-sector, land-cover, and traffic evidence

Morning-peak F_{ff} differed substantially among the eight wind sectors (Fig. 8a). The NE

https://doi.org/10.5194/egusphere-2026-3381
Preprint. Discussion started: 28 July 2026

sector was highest, with a mean of about 6.16 μmol m^{-2} s^{-1}; the N sector was second, about 4.81 μmol m^{-2} s^{-1}; and the SW sectors also remained relatively high, about 4.46 μmol m^{-2} s^{-1}. The W sector was lowest, about 2.48 μmol m^{-2} s^{-1}. Thus, morning-peak F_{ff} was not enhanced uniformly across all wind directions, but was concentrated in specific source-area directions.

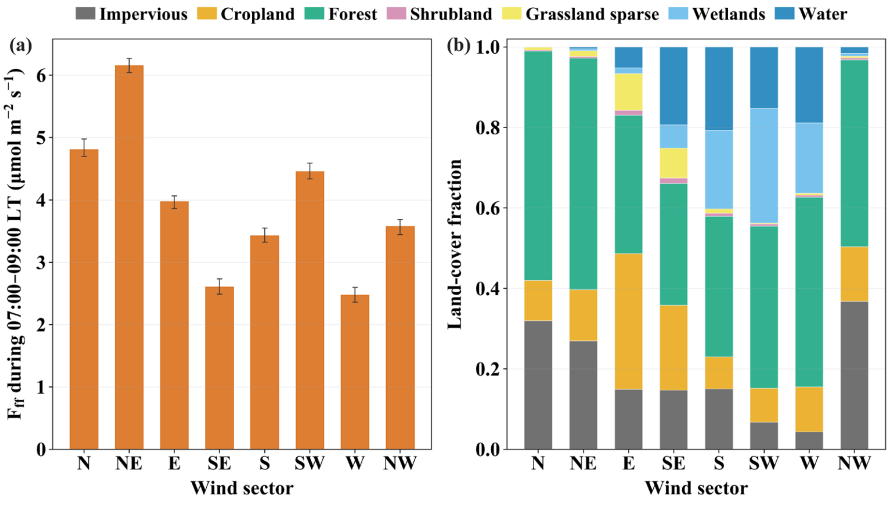

Figure 8. Morning-peak anthropogenic CO_2 flux and footprint-weighted land-cover composition by wind sector at the PY site. **(a)** Mean anthropogenic CO_2 flux (F_{ff}) during 07:00–09:00 LT for eight wind-direction sectors, using the same 45° sector classification as in Fig. 3. Error bars indicate the interquartile range (Q25–Q75). **(b)** Corresponding footprint-weighted land-cover composition for each sector during the same morning-peak period.

Footprint-weighted land cover shows that high F_{ff} is broadly consistent with urbanized and mixed activity source areas, but is not controlled by impervious fraction alone (Fig. 8b). The N, NE, and NW sectors had impervious fractions of about 33 %, 27 %, and 37 %, respectively, and also high forest fractions of about 46 %–58 %. This indicates that urban green space, roads, and hard surfaces are closely interwoven in the PY source area. The simultaneously high F_{ff} and high impervious fraction in the NE and N sectors support their urban-activity source character. In contrast, the SW sector had a lower impervious fraction but higher F_{ff}, suggesting that local road nodes, parking entrances, campus gates, or short-term traffic aggregation areas can generate strong anthropogenic CO_2 signals even under a lower impervious-background fraction in

https://doi.org/10.5194/egusphere-2026-3381
Preprint. Discussion started: 28 July 2026

mixed urban source areas.

Road-congestion indicators provide additional supporting evidence for this interpretation (Fig. 9). The extended congestion dataset covers 331 hourly road snapshots from 23:00 LT on 6 May to 13:00 LT on 24 May 2026, including 713 road segments within approximately 1.5 km of the PY site. These data are not synchronous with the main EC analysis period (2023–2024) and are therefore not used for hourly validation of F_{ff} or for conversion to traffic CO_2 emission fluxes. Instead, they provide an auxiliary description of typical road-traffic timing, directional contrast, and line-source distribution around the PY university-town area. Details on data source, representativeness, and processing are given in Sect. S8.

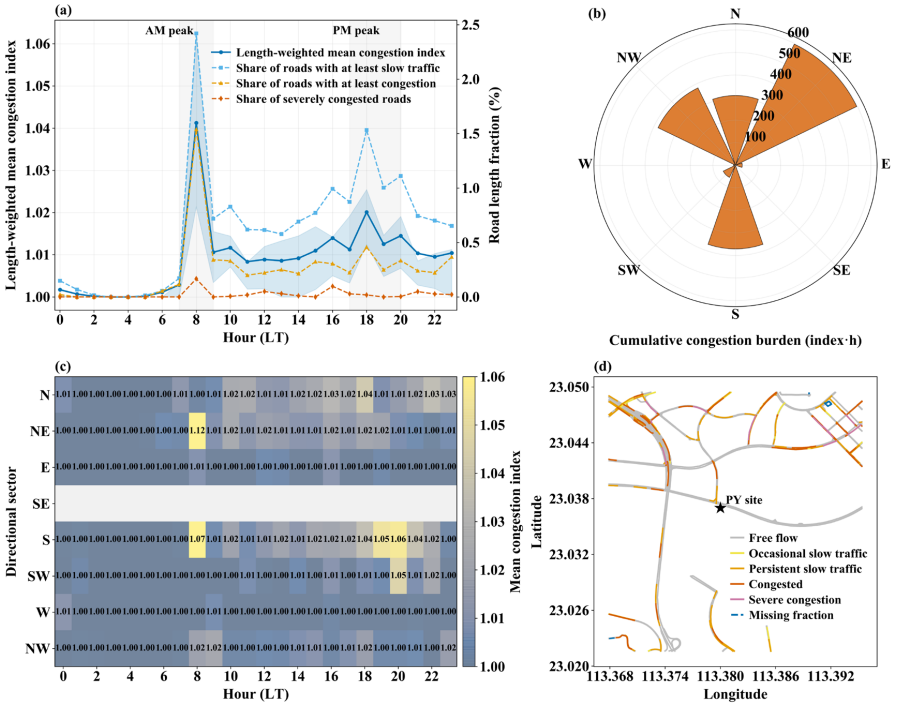

Figure 9. Traffic-activity indicators used to interpret the temporal, directional, and spatial behavior of the PY anthropogenic CO_2 flux (F_{ff}). **(a)** Diurnal variation of the length-weighted mean congestion index and the fractions of road length with at least slow traffic, at least congestion, and severe congestion. **(b)** Eight-sector rose plot of the cumulative congestion burden (index·h). **(c)** Hour × directional-sector heat map of the mean congestion index. **(d)** Spatial distribution of road-segment mean congestion class surrounding the PY site, used to identify the road segments responsible for the directional congestion patterns shown in panel (b).

https://doi.org/10.5194/egusphere-2026-3381
Preprint. Discussion started: 28 July 2026

Figure 9a shows a clear traffic-activity rhythm. The length-weighted mean congestion index and the fractions of road length with slow or congested traffic increased during the morning and evening traffic-relevant periods, with the strongest and sharpest enhancement around 08:00 LT and a broader but weaker increase after approximately 16:00 LT. The overall congestion amplitude remained modest, indicating that most roads were free-flowing or only mildly slow during the monitoring period. Nevertheless, the timing and relative strength of the congestion enhancements are consistent with the high-value windows of F_{ff} and NO_x, supporting the interpretation that the double-peak structure of F_{ff} is broadly associated with road-traffic activity.

The directional traffic evidence further supports the sectoral interpretation of F_{ff}. The cumulative congestion burden is unevenly distributed among directions and is strongest in the NE sector, with additional contributions from the N, NW, and S sectors (Fig. 9b). The hour-sector heat map shows a pronounced NE morning enhancement around 08:00 LT, consistent with the highest morning-peak F_{ff} in the NE sector (Fig. 8a). The S and SW sectors show stronger congestion from evening to nighttime, helping explain why traffic-related activity can also contribute to relatively high F_{ff} in these directions despite their lower impervious-background fraction. The road-segment map further links these directional patterns to specific road corridors near PY, especially to the NE and along several southern to southwestern road sections (Figs. 9d and S8).

Taken together, Figs. 8, 9, and S8 indicate that spatial differences in morning-peak F_{ff} at PY reflect the combined effects of urbanized land cover, local road or gate-related line sources, and dynamic EC footprints. The agreement among F_{ff}, pollutant peaks, footprint-weighted land cover, sectoral congestion burden, and road-segment congestion patterns strengthens the anthropogenic interpretation of F_{ff}, while non-monotonic relationships among these indicators reflect the complexity of mixed university-town source areas.

3.4.3 Inventory magnitude context and spatial-allocation implications

Figure 10 compares PY F_{ff} with footprint-weighted monthly estimates from three widely used bottom-up inventories: the Open-Data Inventory for Anthropogenic

https://doi.org/10.5194/egusphere-2026-3381
Preprint. Discussion started: 28 July 2026

Carbon Dioxide (ODIAC; Oda et al., 2018), the Emissions Database for Global Atmospheric Research (EDGAR; Crippa et al., 2024), and the Multi-resolution Emission Inventory model for Climate and air pollution research (MEIC; Xu et al., 2024). Detailed information on the inventories and calculation procedure is provided in Sect. S5. Inventory central estimates are generally higher than the observation-inferred F_{ff}: EDGAR is about 9–11 μmol m^{-2} s^{-1}, MEIC about 13–15 μmol m^{-2} s^{-1}, and ODIAC about 16–23 μmol m^{-2} s^{-1}, whereas monthly PY F_{ff} is about 2.59–4.29 μmol m^{-2} s^{-1}. This several-fold difference should be interpreted in the context of both spatial-support mismatch and spatial-proxy mismatch. Global and regional gridded inventories do not directly observe emissions within the EC footprint. Instead, they allocate national, regional, or sectoral activity data to grid cells using proxy variables such as population density, night-time lights, road networks, point-source locations, and sectoral activity distributions. ODIAC distributes non-point fossil-fuel CO_2 emissions mainly using satellite-observed night-time lights after separately treating large point sources (Oda et al., 2018). EDGAR uses sector-specific spatial proxies, including population, road networks, facility locations, and land-use information, to construct gridded emissions (Crippa et al., 2024). MEIC improves sectoral and subnational representation, but its gridded fields are still spatially allocated inventory estimates rather than direct footprint-scale observations (Xu et al., 2024). This proxy-allocation issue is particularly relevant for the PY footprint. The Guangzhou Higher Education Mega Center is a high-population-density and brightly lit urban functional zone with dense road infrastructure, but its on-site fossil-fuel combustion intensity per capita is likely lower than that of industrial, commercial, or heavily trafficked urban cores (Sect. 3.3.1). Buildings within the source area mainly rely on externally supplied electricity, and many roads are low-speed campus-service roads or have restricted access (Sect. S8). Population density, night-time lights, and road density may therefore over-represent local combustion emissions when used as spatial allocation proxies. In such a setting, footprint-weighted inventory values can be several times larger than the EC-inferred F_{ff} because broader urban emissions are partly assigned to a high-proxy-intensity functional zone with relatively low on-site combustion.

https://doi.org/10.5194/egusphere-2026-3381
Preprint. Discussion started: 28 July 2026

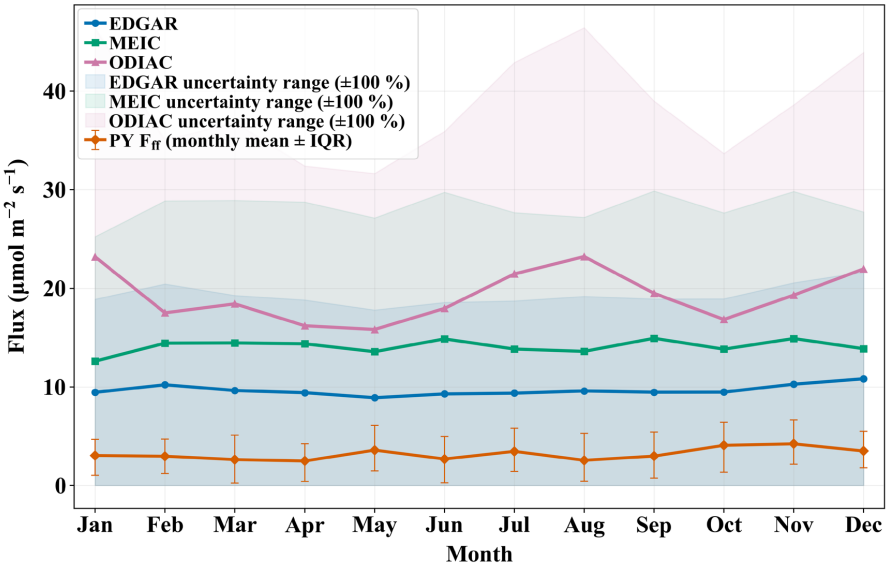

Figure 10. Monthly comparison between the PY anthropogenic CO_2 flux (F_{ff}) and footprint-aligned bottom-up inventory estimates. The PY observation represents the CH0 main scenario with the base human-respiration setting and is summarized as the monthly mean with the interquartile range (Q25–Q75). EDGAR, MEIC, and ODIAC are shown as monthly central estimates. The shaded bands show an illustrative ±100 % envelope to visualize broad urban-grid inventory uncertainty, rather than inventory-specific confidence intervals.

To illustrate the possible magnitude of city- or grid-scale inventory differences, Fig. 10 uses a ± 100 % range as an illustrative uncertainty envelope, not as an inventory-specific confidence interval. Although the inventory central estimates are several times higher than PY F_{ff}, the observation-inferred monthly F_{ff} remains within the illustrative ±100 % inventory envelopes shown in Fig. 10. This indicates that the discrepancy is large, but still falls within the broad local/grid-scale uncertainty context reported for urban fossil-fuel CO_2 inventories. Previous studies show that fossil-fuel CO_2 inventory uncertainty is strongly scale dependent: it is relatively small at national or regional aggregate scales but can increase substantially at city, neighborhood, or 0.1° grid scales. Gately and Hutyra (2017) reported that different inventories can differ by 50 %–250 % at city scale and that many 0.1° grids differ by more than 100 %. More importantly for the present study, spatial proxy variables themselves can introduce local positive bias when they do not represent the true distribution of combustion activity. Squires et al.

https://doi.org/10.5194/egusphere-2026-3381
Preprint. Discussion started: 28 July 2026

(2020) compared EC measurements of traffic-dominated NO_x and CO fluxes in central Beijing with MEIC and found that MEIC substantially overestimated emissions within the EC footprint, providing direct evidence that proxy-based inventories can have positive biases for traffic-related emissions in Chinese urban centers. Wu et al. (2022) similarly emphasized that EC-based source decomposition is needed to evaluate high-resolution urban CO_2 inventories at the footprint scale rather than relying on net CO_2 flux or gridded inventories alone.

From this perspective, the lower PY F_{ff} relative to EDGAR, MEIC, and ODIAC should not be interpreted simply as evidence that the EC-based estimate is biased low. It more likely reflects a combination of footprint-scale ecological correction, local functional-zone representativeness, and proxy-based spatial allocation errors in gridded inventories. A model-side contribution to the difference is also possible. Under the present sign convention, underestimated GPP or overestimated R_{eco} would shift F_{ff} downward, whereas overestimated GPP would shift F_{ff} upward. The potential influence of ecological-correction uncertainty on F_{ff} magnitude is examined in Sect. 3.5. The inventory comparison therefore provides a magnitude reference and a diagnostic of spatial-allocation plausibility, rather than numerical validation of either the inventories or F_{ff}. The large inventory–F_{ff} difference at PY further indicates that spatial-proxy mismatch can be substantial in special-function urban zones, where population density, night-time lights, and road density do not necessarily scale with local fossil-fuel combustion intensity.

Overall, the anthropogenic-emission attribution of PY F_{ff} is constrained by multiple independent lines of evidence. Temporally, F_{ff} is consistent with the diurnal patterns of NO_x and CO, and the morning-peak enhancement is close to that of NO_x. Spatially, high F_{ff} in the eight-sector analysis occurs mainly in NE, N, and SW directions, where urban activity or road-traffic contributions are stronger, and is broadly consistent with footprint-weighted land cover, sectoral congestion load, and road-segment congestion distribution. In magnitude, F_{ff} is lower than bottom-up inventory central estimates, but this comparison provides an urban-emission background, a plausibility boundary, and a diagnostic of possible proxy-allocation mismatch in a

https://doi.org/10.5194/egusphere-2026-3381
Preprint. Discussion started: 28 July 2026

special-function urban zone. Thus, PY F_{ff} is not an isolated residual produced only by model calculation. Rather, it is an ecologically corrected anthropogenic CO_2 flux estimate supported by multiple consistency checks across pollutant timing, source-area structure, traffic activity, and inventory magnitude context.

3.5 Uncertainty sources and robustness of F_{ff}

Donor–target parameter migration is the core structural assumption of the framework. Its uncertainty arises from differences in canopy structure, vegetation composition, soil moisture, substrate availability, and management intensity between CH and PY, which cannot be fully captured by EVI. Because F_{ff} is obtained after subtracting migrated biogenic fluxes and human respiration from the storage-corrected net flux, we treat the migrated biogenic components as constrained approximations and evaluate how key assumptions affect F_{ff}. This uncertainty is especially relevant for R_{eco}, for which EVI_{fp} mainly constrains the vegetation-associated respiratory capacity within the footprint but cannot fully represent soil moisture, substrate supply, irrigation, or management-driven differences between CH and PY. These unresolved R_{eco} controls are treated as part of the structural boundary of the donor–target migration framework, rather than as separately identifiable uncertainty sources in the present sensitivity design. The analysis focuses on whether sensitivity scenarios mainly change the absolute magnitude of F_{ff} or also alter its positive sign across seasons and its morning–evening peak structure.

3.5.1 Relative contributions of uncertainty sources

Figure 11 summarizes the mean F_{ff} offsets of each sensitivity scenario relative to the baseline. Overall, GPP model structure is the dominant source of variation in F_{ff} magnitude. The pure saturating light-response structure and the saturating + VPD inhibition structure reduce mean F_{ff} by about 0.546 and 0.547 μmol m^{-2} s^{-1}, respectively, clearly larger than the effects of other processing steps. By comparison, CH-side shortwave-radiation perturbations of −10 % and +10 % change mean F_{ff} by about +0.092 and −0.085 μmol m^{-2} s^{-1}, respectively; the EVI 5 d window reduces F_{ff} by about

https://doi.org/10.5194/egusphere-2026-3381
Preprint. Discussion started: 28 July 2026

0.077 μmol m^{-2} s^{-1}; the u* threshold within ±20 % changes F_{ff} by about −0.068 to +0.021 μmol m^{-2} s^{-1}; Scheme B and weak daytime-respiration inhibition have effects of about ±0.041 μmol m^{-2} s^{-1}; and the ±10 % storage-flux perturbation is close to zero, within about 0.005 μmol m^{-2} s^{-1}.

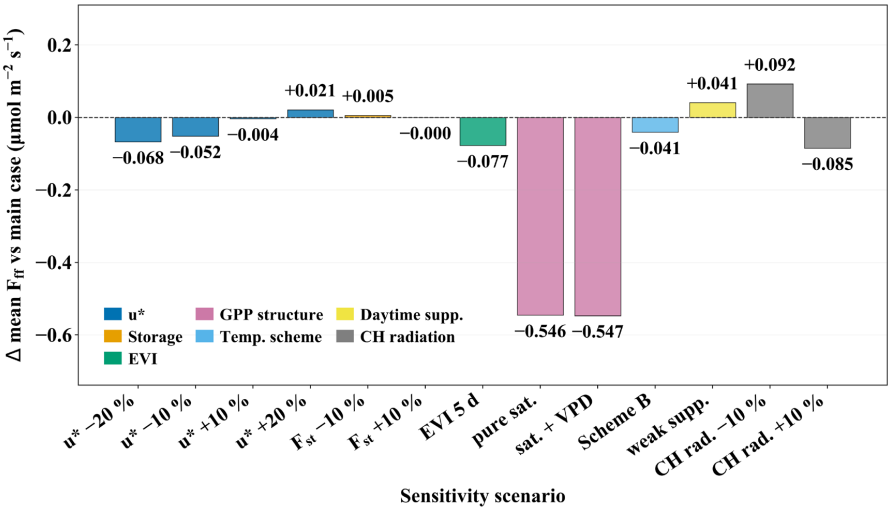

Figure 11. Module sensitivity of the PY anthropogenic CO_2 flux (F_{ff}) relative to the main case. Bars show the difference in the overall mean F_{ff} between each sensitivity scenario and the main case, using the base human-respiration setting. Colors denote uncertainty modules, including u* threshold, storage correction, EVI temporal window, GPP model structure, temperature-group scheme, daytime respiration suppression, and CH-only shortwave-radiation perturbation.

This result shows that uncertainty in PY F_{ff} mainly arises from the biogenic-uptake term, especially the structural estimation of daytime GPP, rather than from small additive terms such as storage flux or u* filtering. This directly addresses the inventory-comparison concern raised in Sect. 3.4.3: ecological-correction uncertainty can shift the absolute magnitude of F_{ff}, but the tested biogenic-correction scenarios do not remove the several-fold gap between F_{ff} and the footprint-weighted inventory central estimates. The CH-only radiation-input perturbation has a larger effect than storage flux and daytime-respiration inhibition, but remains substantially smaller than the GPP-structure difference. Thus, CH radiation representativeness is an input uncertainty that should be reported, but it is not the dominant factor controlling the F_{ff} conclusions. This dominance is expected because GPP is the key daytime subtraction term in the F_{ff}

https://doi.org/10.5194/egusphere-2026-3381
Preprint. Discussion started: 28 July 2026

calculation; different light-response structures directly alter the daytime biogenic-uptake estimate and therefore the amplitude of diurnal F_{ff} variation. Previous EC flux-partitioning studies also show that nighttime respiration extrapolation and daytime GPP model structure can strongly affect NEE partitioning, especially during periods of strong daytime biogenic uptake, when structural differences are often more important than random parameter error (Reichstein et al., 2005; Lasslop et al., 2010; Desai et al., 2008). It is also notable that the pure saturating structure and the saturating + VPD inhibition structure have almost identical effects on F_{ff}. This is consistent with the CH-side model comparison in Sect. 3.2, which showed that the explicit VPD inhibition term did not add explanatory power beyond the pure saturating structure in the present dataset. Figure 11 therefore not only identifies GPP structure as the main uncertainty source, but also further supports the temperature-stratified light-response structure as the baseline scheme.

3.5.2 Robustness of diurnal and seasonal patterns

Figure 12a compares the diurnal spread of F_{ff} among the baseline and 13 sensitivity or structural-alternative scenarios with parameter-bootstrap uncertainty. The scenario spread is larger than the bootstrap uncertainty during most hours. At the hourly scale, the mean scenario q90–q10 spread is about 0.47 μmol m^{-2} s^{-1}, whereas the mean bootstrap q90–q10 spread is about 0.21 μmol m^{-2} s^{-1}; the former is about 2.3 times the latter. Thus, within the present framework, model structure and processing-scenario choices explain the overall uncertainty in F_{ff} more strongly than bootstrap resampling of parameters alone. This result is consistent with previous flux-partitioning studies showing that parameter-estimation error is important, but light-response structure and data-processing choices can produce systematic shifts in partitioning results (Papale et al., 2006; Lasslop et al., 2010; Richardson and Hollinger, 2007).

In terms of diurnal variation, scenario spread is more pronounced during the morning and evening peaks and the daytime transition periods. The largest scenario q90–q10 spread occurs at 16:00, 17:00, and 08:00, corresponding to the afternoon transition when biogenic uptake weakens, the evening peak, and the morning peak. This

https://doi.org/10.5194/egusphere-2026-3381
Preprint. Discussion started: 28 July 2026

gives the F_{ff} uncertainty a clear process meaning: at night, GPP is close to zero and F_{ff} is mainly controlled by net flux and respiration terms; during daytime and evening, it is affected by both ecological-correction choices and anthropogenic-activity rhythms, so scenario differences are larger. Despite these amplitude differences, the morning and evening peaks persist in all scenarios, and the relatively low midday F_{ff} pattern is not changed. Thus, scenario uncertainty mainly affects F_{ff} magnitude after daytime biogenic-uptake correction, rather than the presence of a diurnal structure associated with urban anthropogenic activity.

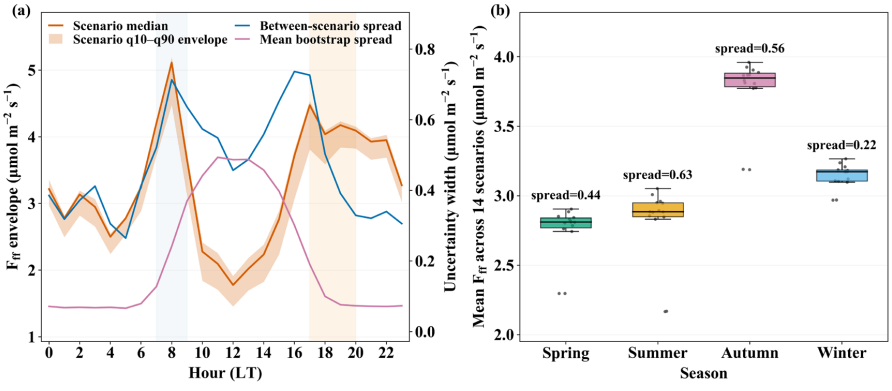

Figure 12. Integrated uncertainty-spread diagnostics for the PY anthropogenic CO_2 flux (F_{ff}). **(a)** Diurnal comparison between the scenario envelope and bootstrap uncertainty under the base human-respiration setting. The colored uncertainty ribbon, bounded by the q10 and q90 lines, represents the envelope of hourly mean F_{ff} across the 14 sensitivity scenarios; the solid line shows the scenario median. The between-scenario spread (q90–q10) and the mean within-scenario bootstrap spread (q90–q10) are also shown. Pale vertical background bands highlight the morning (07:00–09:00 LT) and evening (17:00–20:00 LT) traffic-relevant periods. **(b)** Seasonal distributions of scenario-mean F_{ff} across the 14 CH scenarios under the base human-respiration setting. Boxplots summarize the spread among scenarios for each season, and points denote individual scenario means.

Figure 12b further shows that the seasonal uncertainty in F_{ff} is also linked to biogenic processes. Across the 14 scenarios, the scenario range is largest in summer, followed by autumn, and smallest in winter. This is consistent with the seasonality of the biogenic components: warm-season GPP and R_{eco} are stronger, so ecological model structure and radiation input have larger effects on F_{ff}. In winter, biogenic processes are weaker, and differences caused by model structure and input perturbations are reduced. In other words, F_{ff} uncertainty is not randomly distributed. It is concentrated in warm-

https://doi.org/10.5194/egusphere-2026-3381
Preprint. Discussion started: 28 July 2026

season and daytime periods, when ecological correction is strongest and component separation is most difficult.

This pattern also provides a boundary test for the CH-to-PY migration assumption: scenario spread is largest when ecological correction is strongest, but the positive sign across seasons and the morning–evening peak structure remain stable.

3.5.3 Interpretive boundaries of F_{ff}

Core structural scenarios further clarify the interpretive boundary of F_{ff} (Fig. S9a). The baseline scheme, Scheme B, and the weak daytime-respiration-inhibition scenario produce similar diurnal shapes, whereas the pure saturating and saturating + VPD inhibition structures yield lower F_{ff} values, especially during daytime and evening. Thus, GPP structure mainly controls the inferred magnitude of F_{ff}, while the morning peak, midday low, and evening peak remain robust. This supports using F_{ff} as a footprint-scale anthropogenic-activity signal, but its absolute value remains conditional on the ecological model structure and donor–target migration assumptions.

Human-respiration sensitivity provides a separate boundary on the non-fossil anthropogenic term (Fig. S9b–c). Even when human respiration is set to 0.5 or 1.5 times the baseline, the mean change in F_{ff} is only about ±0.01 μmol m^{-2} s^{-1}, and the maximum hourly effect is about ±0.026 μmol m^{-2} s^{-1}. Human respiration should therefore be explicitly subtracted, but it is not a dominant uncertainty under the current PY source-area background. Overall, PY F_{ff} is best interpreted as an ecologically constrained, footprint-scale anthropogenic CO_2 flux estimate: robust as a relative temporal and source-area signal, but not a model-independent observation or direct inversion of local traffic or inventory emissions.

4 Conclusions

Using paired EC observations from the CH and PY sites in Guangzhou, this study developed a footprint-informed ecological parameter-migration framework for partitioning CO_2 fluxes in mixed urban source areas. The framework uses CH as a relatively clean ecological donor, transfers vegetation-normalized ecological

https://doi.org/10.5194/egusphere-2026-3381
Preprint. Discussion started: 28 July 2026

parameters to PY using dynamic footprints and footprint-weighted enhanced vegetation index (EVI_{fp}), and estimates footprint-scale anthropogenic CO_2 flux (F_{ff}) after ecological and human-respiration corrections.

The CH-to-PY migration was supported by a consistent ecological evidence chain. The two sites share a similar regional climatic and phenological background but differ strongly in vegetation cover and anthropogenic influence. After EVI_{fp}-based scaling, the migrated PY gross primary productivity (GPP) and ecosystem respiration (R_{eco}) showed plausible diurnal and seasonal patterns, with magnitudes consistent with reported urban green-space and mixed-source fluxes. These results support the donor–target design as an ecologically consistent constraint on biogenic components, while the migrated fluxes should still be interpreted as constrained approximations rather than directly validated ecological observations.

The partitioned components reveal how biogenic and anthropogenic processes jointly shape net CO_2 exchange at the urban target site. PY remained a net CO_2 source overall, but daytime storage-corrected net CO_2 flux (F_{cr}) could approach neutral values or become weakly negative when GPP was strong. After ecological correction, F_{ff} remained positive throughout the day, with hourly means of 1.80–5.14 μmol m^{-2} s^{-1} and a clear morning peak and weaker evening peak. Thus, urban EC net flux cannot be interpreted directly as anthropogenic emissions because vegetation uptake can mask part of the anthropogenic signal.

The inferred F_{ff} showed temporal and source-area patterns consistent with footprint-scale anthropogenic activity, including diurnal agreement with combustion-related tracers and high morning-peak values in sectors with stronger urban activity or traffic-related source contributions. Footprint-weighted inventory comparisons provided an order-of-magnitude context, but should not be interpreted as strict inventory validation. The large inventory–F_{ff} difference at PY further suggests that proxy-based spatial allocation can be problematic in special-function urban zones, where population density, night-time lights, and road density do not necessarily scale with local fossil-fuel combustion intensity.

The uncertainty analysis showed that F_{ff} was most sensitive to GPP light-response

https://doi.org/10.5194/egusphere-2026-3381
Preprint. Discussion started: 28 July 2026

structure, whereas other input, screening, parameterization, storage, and human-respiration choices had smaller effects. Scenario differences mainly affected the absolute magnitude of F_{ff}, especially during daytime and the warm season, but did not change its positive sign across seasons or its morning–evening peak structure. F_{ff} should therefore be interpreted as an ecologically constrained, footprint-scale anthropogenic CO_2 flux estimate, not as a model-independent direct emission observation.

Several limitations remain. The uncertainty framework is based on controlled sensitivity scenarios rather than a complete probability distribution of all error sources. The CH-to-PY migration depends on ecological similarity, EVI_{fp}-based scaling, footprint and remote-sensing representativeness, CH-side radiation input, and site-level microclimatic contrasts. These factors define the main boundary for extending the framework to other urban sites. F_{ff} should be used as a tower-footprint-scale observational constraint and relative-change indicator, rather than as a direct replacement for city-total inventories. Future work combining multi-site EC networks with traffic, energy-use, mobile, isotopic, or auxiliary tracer observations would help further test and extend this framework.

This study demonstrates the feasibility of an EC-based CO_2 flux-partitioning approach for urban areas where green spaces and anthropogenic sources are highly mixed. By combining standard EC CO_2 fluxes with dynamic footprints, high-resolution land cover, and open satellite vegetation-index products, the framework lowers the observational barrier for source–sink partitioning in data-scarce and rapidly urbanizing regions, including many cities in the Global South. Beyond flux partitioning, it helps reveal anthropogenic CO_2 emission signals masked by biogenic processes, while providing footprint-scale constraints for diagnosing potential spatial-proxy mismatch in gridded inventories and informing urban carbon-monitoring network design.

Code and data availability. The source code for the two-dimensional flux-footprint model used in this study is available at https://footprint.kljun.net (Kljun et al., 2015). The global 10 m land-cover product GLC_FCS10 used in this study has been published on Zenodo and can be accessed at https://doi.org/10.5281/zenodo.14729665 (last access: 25 May 2026) (Zhang et al., 2025). The global 10 m canopy-height product used in this

https://doi.org/10.5194/egusphere-2026-3381
Preprint. Discussion started: 28 July 2026

study is publicly available and can be downloaded from https://langnico.github.io/globalcanopyheight/assets/tile_index.html (Lang et al., 2023). The Harmonized Landsat Sentinel-2 (HLS) 30 m vegetation-index products used in this study are publicly available at https://doi.org/10.5067/HLS/HLSL30_VI.002 and https://doi.org/10.5067/HLS/HLSS30.002 (last access: 25 May 2026) (Neigh, 2021; Neigh, 2025). The road-traffic congestion and vector building-height data around the PY site used in this study are available from https://lbs.amap.com (last access: 25 May 2026). The national hourly population-density spatial-distribution dataset used in this study can be accessed at https://doi.org/10.12078/2022091601 (Xu, 2022). Additional data and information used in this study are available from the corresponding author upon request.

Author contributions. JWZ and ML designed the study. JWZ, YJL, YFY, CLP, HBH, BH, XFL, YYH, YWP, CLC, CW, ZZ, and ML contributed to data collection and data analysis. JWZ designed and performed the model simulations. JWZ and ML wrote the paper with contributions from all coauthors. All the authors revised the paper and edited the text.

Competing interests. The contact author has declared that none of the authors has any competing interests.

Disclaimer. Publisher's note: Copernicus Publications remains neutral with regard to jurisdictional claims made in the text, published maps, institutional affiliations, or any other geographical representation in this paper. The authors bear the ultimate responsibility for providing appropriate place names. Views expressed in the text are those of the authors and do not necessarily reflect the views of the publisher.

Acknowledgements. The authors would like to thank the personnel who participated in data collection, instrument maintenance, and logistic support during the field campaign.

Financial support. This research has been supported by the National Natural Science Foundation of China (grant no. 42477273) and the National Key R&D Program of China (grant no. 2022YFE0209500).

References

Aubinet, M., Chermanne, B., Vandenhaute, M., Longdoz, B., Yernaux, M., and Laitat, E.: Long term carbon dioxide exchange above a mixed forest in the Belgian Ardennes, Agr. Forest Meteorol., 108, 293-315, https://doi.org/10.1016/S0168-1923(01)00244-1, 2001.

Baldocchi, D. D.: Assessing the eddy covariance technique for evaluating carbon dioxide

https://doi.org/10.5194/egusphere-2026-3381
Preprint. Discussion started: 28 July 2026

exchange rates of ecosystems: past, present and future, Global Change Biol., 9, 479-492, https://doi.org/10.1046/j.1365-2486.2003.00629.x, 2003.

Crawford, B. and Christen, A.: Spatial source attribution of measured urban eddy covariance CO_2 fluxes, Theor. Appl. Climatol., 119, 733-755, https://doi.org/10.1007/s00704-014-1124-0, 2015.

Crawford, B., Grimmond, C. S. B., and Christen, A.: Five years of carbon dioxide fluxes measurements in a highly vegetated suburban area, Atmos. Environ., 45, 896-905, https://doi.org/10.1016/j.atmosenv.2010.11.017, 2011.

Crippa, M., Guizzardi, D., Pagani, F., Banja, M., Muntean, M., Schaaf, E., Monforti-Ferrario, F., Becker, W. E., Quadrelli, R., Risquez Martin, A., Taghavi-Moharamli, P., Köykkä, J., Grassi, G., Rossi, S., Melo, J., Oom, D., Branco, A., San-Miguel, J., Manca, G., Pisoni, E., Vignati, E., and Pekar, F.: GHG emissions of all world countries, Publications Office of the European Union, https://doi.org/10.2760/4002897, 2024.

Decina, S. M., Hutyra, L. R., Gately, C. K., Getson, J. M., Reinmann, A. B., Short Gianotti, A. G., and Templer, P. H.: Soil respiration contributes substantially to urban carbon fluxes in the greater Boston area, Environmental Pollution, 212, 433-439, https://doi.org/10.1016/j.envpol.2016.01.012, 2016.

Desai, A. R., Richardson, A. D., Moffat, A. M., Kattge, J., Hollinger, D. Y., Barr, A., Falge, E., Noormets, A., Papale, D., Reichstein, M., and Stauch, V. J.: Cross-site evaluation of eddy covariance GPP and RE decomposition techniques, Agr. Forest Meteorol., 148, 821-838, https://doi.org/10.1016/j.agrformet.2007.11.012, 2008.

Foken, T., Göockede, M., Mauder, M., Mahrt, L., Amiro, B., and Munger, W.: Post-Field Data Quality Control, in: Handbook of Micrometeorology: A Guide for Surface Flux Measurement and Analysis, edited by: Lee, X., Massman, W., and Law, B., Springer Netherlands, Dordrecht, 181-208, https://10.1007/1-4020-2265-4_9, 2004.

Gately, C. K. and Hutyra, L. R.: Large Uncertainties in Urban-Scale Carbon Emissions, J. Geophys. Res.-Atmos., 122, 11242–11260, https://doi.org/10.1002/2017jd027359, 2017.

Gourdji, S. M., Karion, A., Lopez-Coto, I., Ghosh, S., Mueller, K. L., Zhou, Y., Williams, C. A., Baker, I. T., Haynes, K. D., and Whetstone, J. R.: A Modified Vegetation Photosynthesis and Respiration Model (VPRM) for the Eastern USA and Canada, Evaluated With Comparison to Atmospheric Observations and Other Biospheric Models, J. Geophys. Res.-Biogeosci., 127, e2021JG006290, https://doi.org/10.1029/2021JG006290, 2022.

Grimmond, C. S. B. and Oke, T. R.: Aerodynamic Properties of Urban Areas Derived from Analysis of Surface Form, J. Appl. Meteorol., 38, 1262-1292, https://doi.org/10.1175/1520-0450(1999)038<1262:APOUAD>2.0.CO;2, 1999.

Guo, S., Hu, M., Zamora, M. L., Peng, J., Shang, D., Zheng, J., Du, Z., Wu, Z., Shao, M., and Zeng, L.: Elucidating severe urban haze formation in China, P. Natl. Acad. Sci. USA, 111, 17373-17378, https://doi.org/10.1073/pnas.1419604111, 2014.

Hardiman, B. S., Wang, J. A., Hutyra, L. R., Gately, C. K., Getson, J. M., and Friedl, M. A.: Accounting for urban biogenic fluxes in regional carbon budgets, Sci. Total Environ., 592, 366-372, https://doi.org/10.1016/j.scitotenv.2017.03.028, 2017.

Hilland, R., Hashemi, J., Stagakis, S., Brunner, D., Constantin, L., Kljun, N., Kunz, A. K., Molinier, B., Hammer, S., Emmenegger, L., and Christen, A.: Sectoral attribution of greenhouse gas and pollutant emissions using multi-species eddy covariance on a tall tower

https://doi.org/10.5194/egusphere-2026-3381
Preprint. Discussion started: 28 July 2026

in Zurich, Switzerland, Atmos. Chem. Phys., 25, 14279-14299, https://doi.org/10.5194/acp-25-14279-2025, 2025.

Horne, J. P., Richardson, S. J., Murphy, S. L., Kenion, H. C., Haupt, B. J., Ahlswede, B. J., Miles, N. L., and Davis, K. J.: The INFLUX network – eddy covariance in and around an urban environment, Earth Syst. Sci. Data, 18, 823-843, https://doi.org/10.5194/essd-18-823-2026, 2026.

Huete, A., Didan, K., Miura, T., Rodriguez, E. P., Gao, X., and Ferreira, L. G.: Overview of the radiometric and biophysical performance of the MODIS vegetation indices, Remote Sens. Environ., 83, 195-213, https://doi.org/10.1016/S0034-4257(02)00096-2, 2002.

Ishidoya, S., Sugawara, H., Terao, Y., Kaneyasu, N., Aoki, N., Tsuboi, K., and Kondo, H.: O_2:CO_2 exchange ratio for net turbulent flux observed in an urban area of Tokyo, Japan, and its application to an evaluation of anthropogenic CO_2 emissions, Atmos. Chem. Phys., 20, 5293-5308, https://doi.org/10.5194/acp-20-5293-2020, 2020.

Järvi, L., Nordbo, A., Junninen, H., Riikonen, A., Moilanen, J., Nikinmaa, E., and Vesala, T.: Seasonal and annual variation of carbon dioxide surface fluxes in Helsinki, Finland, in 2006–2010, Atmos. Chem. Phys., 12, 8475-8489, https://doi.org/10.5194/acp-12-8475-2012, 2012.

Järvi, L., Havu, M., Ward, H. C., Bellucco, V., McFadden, J. P., Toivonen, T., Heikinheimo, V., Kolari, P., Riikonen, A., and Grimmond, C. S. B.: Spatial Modeling of Local-Scale Biogenic and Anthropogenic Carbon Dioxide Emissions in Helsinki, J. Geophys. Res.-Atmos., 124, 8363-8384, https://doi.org/10.1029/2018JD029576, 2019.

Juchem, H., Maier, F., Levin, I., Jordan, A., Pöhler, D., Rosendahl, C., Della Coletta, J., Preunkert, S., and Hammer, S.: Challenges and benefits of using NO_x as a quantitative proxy for fossil fuel CO_2 in an urban area based on radiocarbon measurements, Atmos. Chem. Phys., 25, 18373-18388, https://doi.org/10.5194/acp-25-18373-2025, 2025.

Keenan, T. F., Migliavacca, M., Papale, D., Baldocchi, D., Reichstein, M., Torn, M., and Wutzler, T.: Widespread inhibition of daytime ecosystem respiration, Nat. Ecol. Evol., 3, 407-415, https://doi.org/10.1038/s41559-019-0809-2, 2019.

Kljun, N., Calanca, P., Rotach, M. W., and Schmid, H. P.: A simple two-dimensional parameterisation for Flux Footprint Prediction (FFP), Geosci. Model Dev., 8, 3695-3713, https://doi.org/10.5194/gmd-8-3695-2015, 2015.

Kohonen, K. M., Kolari, P., Kooijmans, L. M. J., Chen, H., Seibt, U., Sun, W., and Mammarella, I.: Towards standardized processing of eddy covariance flux measurements of carbonyl sulfide, Atmos. Meas. Tech., 13, 3957-3975, https://doi.org/10.5194/amt-13-3957-2020, 2020.

Kooijmans, L. M. J., Maseyk, K., Seibt, U., Sun, W., Vesala, T., Mammarella, I., Kolari, P., Aalto, J., Franchin, A., Vecchi, R., Valli, G., and Chen, H.: Canopy uptake dominates nighttime carbonyl sulfide fluxes in a boreal forest, Atmos. Chem. Phys., 17, 11453-11465, https://doi.org/10.5194/acp-17-11453-2017, 2017.

Kunz, A. K., Hammer, S., Aigner, P., Bignotti, L., Borchardt, L., Chen, J., Della Coletta, J., Emmenegger, L., Eritt, M., Gutiérrez, X., Hashemi, J., Hilland, R., Holst, C., Jordan, A., Kljun, N., Kneißl, R., Lan, C., Legendre, V., Levin, I., Loubet, B., Mauder, M., Molinier, B., Preunkert, S., Ramonet, M., Stagakis, S., and Christen, A.: ^{14}C-based separation of fossil and non-fossil CO_2 fluxes in cities using relaxed eddy accumulation: results from tall-tower measurements in Zurich, Paris, and Munich, Atmos. Chem. Phys., 26, 4967-5003,

https://doi.org/10.5194/egusphere-2026-3381
Preprint. Discussion started: 28 July 2026

https://doi.org/10.5194/acp-26-4967-2026, 2026.

Lang, N., Jetz, W., Schindler, K., and Wegner, J. D.: A high-resolution canopy height model of the Earth, Nat Ecol Evol, 7, 1778-1789, https://doi.org/10.1038/s41559-023-02206-6, 2023.

Lasslop, G., Reichstein, M., Papale, D., Richardson, A. D., Arneth, A., Barr, A., Stoy, P., and Wohlfahrt, G.: Separation of net ecosystem exchange into assimilation and respiration using a light response curve approach: critical issues and global evaluation, Global Change Biol., 16, 187-208, https://doi.org/10.1111/j.1365-2486.2009.02041.x, 2010.

Lee, K., Hong, J.-W., Kim, J., and Hong, J.: Partitioning of net CO_2 exchanges at the city-atmosphere interface into biotic and abiotic components, MethodsX, 8, 101231, https://doi.org/10.1016/j.mex.2021.101231, 2021.

Liu, H. Z., Feng, J. W., Järvi, L., and Vesala, T.: Four-year (2006–2009) eddy covariance measurements of CO_2 flux over an urban area in Beijing, Atmos. Chem. Phys., 12, 7881-7892, https://doi.org/10.5194/acp-12-7881-2012, 2012.

Mahadevan, P., Wofsy, S. C., Matross, D. M., Xiao, X., Dunn, A. L., Lin, J. C., Gerbig, C., Munger, J. W., Chow, V. Y., and Gottlieb, E. W.: A satellite-based biosphere parameterization for net ecosystem CO_2 exchange: Vegetation Photosynthesis and Respiration Model (VPRM), Global Biogeochem. Cy., 22, https://doi.org/10.1029/2006GB002735, 2008.

Matese, A., Gioli, B., Vaccari, F. P., Zaldei, A., and Miglietta, F.: Carbon Dioxide Emissions of the City Center of Firenze, Italy: Measurement, Evaluation, and Source Partitioning, J. Appl. Meteorol. Clim., 48, 1940-1947, https://doi.org/10.1175/2009JAMC1945.1, 2009.

Matthews, B. and Schume, H.: Tall tower eddy covariance measurements of CO_2 fluxes in Vienna, Austria, Atmos. Environ., 274, 118941, https://doi.org/10.1016/j.atmosenv.2022.118941, 2022.

Menzer, O. and McFadden, J. P.: Statistical partitioning of a three-year time series of direct urban net CO_2 flux measurements into biogenic and anthropogenic components, Atmos. Environ., 170, 319-333, https://doi.org/10.1016/j.atmosenv.2017.09.049, 2017.

Miller, J. B., Lehman, S. J., Verhulst, K. R., Miller, C. E., Duren, R. M., Yadav, V., Newman, S., and Sloop, C. D.: Large and seasonally varying biospheric CO_2 fluxes in the Los Angeles megacity revealed by atmospheric radiocarbon, P. Natl. Acad. Sci. USA, 117, 26681-26687, https://doi.org/10.1073/pnas.2005253117, 2020.

Monteith, J. L.: Solar radiation and productivity in tropical ecosystems, J. Appl. Ecol., 9, 747-766, https://doi.org/10.2307/2401901, 1972.

Myneni, R. B. and Williams, D. L.: On the relationship between FAPAR and NDVI, Remote Sens. Environ., 49, 200-211, https://doi.org/10.1016/0034-4257(94)90016-7, 1994.

Neigh, C.: HLS Operational Land Imager Vegetation Indices Daily Global 30m v2.0, NASA Land Processes Distributed Active Archive Center [dataset], https://doi.org/10.5067/HLS/HLSL30_VI.002, 2025.

Neigh, C., Ju, J., Roger, J.-C., Skakun, S., Vermote, E., Claverie, M., Dungan, J., Yin, Z., Freitag, B., and Justice, C.: HLS Sentinel-2 Multi-spectral Instrument Surface Reflectance Daily Global 30m v2.0, NASA Land Processes Distributed Active Archive Center [dataset], https://doi.org/10.5067/HLS/HLSS30.002, 2021.

Nordbo, A., Järvi, L., Haapanala, S., Wood, C. R., and Vesala, T.: Fraction of natural area as main predictor of net CO_2 emissions from cities, Geophys. Res. Lett., 39, https://doi.org/10.1029/2012GL053087, 2012.

https://doi.org/10.5194/egusphere-2026-3381
Preprint. Discussion started: 28 July 2026

Oda, T., Maksyutov, S., and Andres, R. J.: The Open-source Data Inventory for Anthropogenic CO_2, version 2016 (ODIAC2016): a global monthly fossil fuel CO_2 gridded emissions data product for tracer transport simulations and surface flux inversions, Earth Syst. Sci. Data, 10, 87-107, https://doi.org/10.5194/essd-10-87-2018, 2018.

Papale, D., Reichstein, M., Canfora, E., Aubinet, M., Bernhofer, C., Longdoz, B., Kutsch, W., Rambal, S., Valentini, R., and Vesala, T.: Towards a more harmonized processing of eddy covariance CO_2 fluxes: algorithms and uncertainty estimation, Biogeosciences, 3, 571–583, https://doi.org/10.5194/bg-3-571-2006, 2006.

Parrish, D. D.: Critical evaluation of US on-road vehicle emission inventories, Atmos. Environ., 40, 2288-2300, https://doi.org/10.1016/j.atmosenv.2005.11.033, 2006.

Pérez-Ruiz, E. R., Vivoni, E. R., and Templeton, N. P.: Urban land cover type determines the sensitivity of carbon dioxide fluxes to precipitation in Phoenix, Arizona, PLoS One, 15, e0228537, https://doi.org/10.1371/journal.pone.0228537, 2020.

Reichstein, M., Falge, E., Baldocchi, D., Papale, D., Aubinet, M., Berbigier, P., Bernhofer, C., Buchmann, N., Gilmanov, T., Granier, A., Grünwald, T., Havránková, K., Ilvesniemi, H., Janous, D., Knohl, A., Laurila, T., Lohila, A., Loustau, D., Matteucci, G., Meyers, T., Miglietta, F., Ourcival, J.-M., Pumpanen, J., Rambal, S., Rotenberg, E., Sanz, M., Tenhunen, J., Seufert, G., Vaccari, F., Vesala, T., Yakir, D., and Valentini, R.: On the separation of net ecosystem exchange into assimilation and ecosystem respiration: review and improved algorithm, Global Change Biol., 11, 1424-1439, https://doi.org/10.1111/j.1365-2486.2005.001002.x, 2005.

Richardson, A. D. and Hollinger, D. Y.: A method to estimate the additional uncertainty in gap-filled NEE resulting from long gaps in the CO_2 flux record, Agr. Forest Meteorol., 147, 199-208, https://doi.org/10.1016/j.agrformet.2007.06.004, 2007.

Rotach, M. W.: On the influence of the urban roughness sublayer on turbulence and dispersion, Atmos. Environ., 33, 4001-4008, https://doi.org/10.1016/S1352-2310(99)00141-7, 1999.

Running, S. W., Nemani, R. R., Heinsch, F. A., Zhao, M., Reeves, M., and Hashimoto, H.: A Continuous Satellite-Derived Measure of Global Terrestrial Primary Production, BioScience, 54, 547-560, https://doi.org/10.1641/0006-3568(2004)054[0547:Acsmog]2.0.Co;2, 2004.

Sabbatini, S., Mammarella, I., Arriga, N., Fratini, G., Graf, A., Hörtnagl, L., Ibrom, A., Longdoz, B., Mauder, M., and Merbold, L.: Eddy covariance raw data processing for CO2 and energy fluxes calculation at ICOS ecosystem stations, International Agrophysics, 32, 495-515, https://doi.org/10.1515/intag-2017-0043, 2018.

Sargent, M., Barrera, Y., Nehrkorn, T., Hutyra, L. R., Gately, C. K., Jones, T., McKain, K., Sweeney, C., Hegarty, J., Hardiman, B., Wang, J. A., and Wofsy, S. C.: Anthropogenic and biogenic CO_2 fluxes in the Boston urban region, P. Natl. Acad. Sci. USA, 115, 7491-7496, https://doi.org/10.1073/pnas.1803715115, 2018.

Sellers, P. J.: Canopy reflectance, photosynthesis and transpiration, International Journal of Remote Sensing, 6, 1335-1372, https://doi.org/10.1080/01431168508948283, 1985.

Soininen, J., Kohonen, K.-M., Rantala, P., Kulmala, L., Aaltonen, H., and Järvi, L.: Carbon uptake of an urban green space inferred from carbonyl sulfide fluxes, npj Clim. Atmos. Sci., 8, https://doi.org/10.1038/s41612-025-00958-5, 2025.

Squires, F. A., Nemitz, E., Langford, B., Wild, O., Drysdale, W. S., Acton, W. J. F., Fu, P., Grimmond, C. S. B., Hamilton, J. F., Hewitt, C. N., Hollaway, M., Kotthaus, S., Lee, J.,

https://doi.org/10.5194/egusphere-2026-3381
Preprint. Discussion started: 28 July 2026

Metzger, S., Pingintha-Durden, N., Shaw, M., Vaughan, A. R., Wang, X., Wu, R., Zhang, Q., and Zhang, Y.: Measurements of traffic-dominated pollutant emissions in a Chinese megacity, Atmos. Chem. Phys., 20, 8737-8761, https://doi.org/10.5194/acp-20-8737-2020, 2020.

Tao, X., Cui, J., Dai, Y., Wang, Z., and Xu, X.: Soil respiration responses to soil physiochemical properties in urban different green-lands: A case study in Hefei, China, International Soil and Water Conservation Research, 4, 224-229, https://doi.org/10.1016/j.iswcr.2016.08.001, 2016.

Turnbull, J. C., Tans, P. P., Lehman, S. J., Baker, D., Conway, T. J., Chung, Y., Gregg, J., Miller, J. B., Southon, J. R., and Zhou, L. X.: Atmospheric observations of carbon monoxide and fossil fuel CO_2 emissions from East Asia, J. Geophys. Res.-Atmos., 116, https://doi.org/10.1029/2011JD016691, 2011.

Ueyama, M. and Takano, T.: A decade of CO_2 flux measured by the eddy covariance method including the COVID-19 pandemic period in an urban center in Sakai, Japan, Environmental Pollution, 304, 119210, https://doi.org/10.1016/j.envpol.2022.119210, 2022.

Velasco, E. and Roth, M.: Cities as Net Sources of CO_2: Review of Atmospheric CO_2 Exchange in Urban Environments Measured by Eddy Covariance Technique, Geography Compass, 4, 1238-1259, https://doi.org/10.1111/j.1749-8198.2010.00384.x, 2010.

Velasco, E., Roth, M., Tan, S., Quak, M., Nabarro, S., and Norford, L.: The role of vegetation in the CO_2 flux from a tropical urban neighbourhood, Atmos. Chem. Phys., 13, 10185-10202, https://doi.org/10.5194/acp-13-10185-2013, 2013.

Wang, L., Yu, M., Ye, S., and Yan, J.: Seasonal patterns of carbon and water flux responses to precipitation and solar radiation variability in a subtropical evergreen forest, South China, Agr. Forest Meteorol., 342, 109760, https://doi.org/10.1016/j.agrformet.2023.109760, 2023.

Ward, H. C., Kotthaus, S., Grimmond, C. S. B., Bjorkegren, A., Wilkinson, M., Morrison, W. T. J., Evans, J. G., Morison, J. I. L., and Iamarino, M.: Effects of urban density on carbon dioxide exchanges: Observations of dense urban, suburban and woodland areas of southern England, Environmental Pollution, 198, 186-200, https://doi.org/10.1016/j.envpol.2014.12.031, 2015.

Webb, E. K., Pearman, G. I., and Leuning, R.: Correction of flux measurements for density effects due to heat and water vapour transfer, Quarterly Journal of the Royal Meteorological Society, 106, 85-100, https://doi.org/10.1002/qj.49710644707, 1980.

Wehr, R., Munger, J. W., McManus, J. B., Nelson, D. D., Zahniser, M. S., Davidson, E. A., Wofsy, S. C., and Saleska, S. R.: Seasonality of temperate forest photosynthesis and daytime respiration, Nature, 534, 680-683, https://doi.org/10.1038/nature17966, 2016.

Wu, D., Lin, J. C., Duarte, H. F., Yadav, V., Parazoo, N. C., Oda, T., and Kort, E. A.: A model for urban biogenic CO_2 fluxes: Solar-Induced Fluorescence for Modeling Urban biogenic Fluxes (SMUrF v1), Geosci. Model Dev., 14, 3633-3661, https://doi.org/10.5194/gmd-14-3633-2021, 2021.

Wu, K., Davis, K. J., Miles, N. L., Richardson, S. J., Lauvaux, T., Sarmiento, D. P., Balashov, N. V., Keller, K., Turnbull, J., and Gurney, K. R.: Source decomposition of eddy-covariance CO_2 flux measurements for evaluating a high-resolution urban CO_2 emissions inventory, Environ. Res. Lett., 17, 074035, https://doi.org/10.1088/1748-9326/ac7c29, 2022.

Wutzler, T., Lucas-Moffat, A., Migliavacca, M., Knauer, J., Sickel, K., Šigut, L., Menzer, O., and Reichstein, M.: Basic and extensible post-processing of eddy covariance flux data with REddyProc, Biogeosciences, 15, 5015-5030, https://doi.org/10.5194/bg-15-5015-2018, 2018.

https://doi.org/10.5194/egusphere-2026-3381
Preprint. Discussion started: 28 July 2026

Xiao, X., Hollinger, D., Aber, J., Goltz, M., Davidson, E. A., Zhang, Q., and Moore, B.: Satellite-based modeling of gross primary production in an evergreen needleleaf forest, Remote Sens. Environ., 89, 519-534, https://doi.org/10.1016/j.rse.2003.11.008, 2004.

Xu, R., Tong, D., Xiao, Q., Qin, X., Chen, C., Yan, L., Cheng, J., Cui, C., Hu, H., and Liu, W.: MEIC-global-CO_2: A new global CO_2 emission inventory with highly-resolved source category and sub-country information, Sci. China Earth Sci, 67, 450-465, https://doi.org/10.1007/s11430-023-1230-3, 2024.

Xu, X.: National hourly population density spatial distribution dataset, Resource and Environmental Science Data Registration and Publication System [dataset], https://doi.org/10.12078/2022091601, 2022.

Xueref-Remy, I., Dieudonné, E., Vuillemin, C., Lopez, M., Lac, C., Schmidt, M., Delmotte, M., Chevallier, F., Ravetta, F., Perrussel, O., Ciais, P., Bréon, F.-M., Broquet, G., Ramonet, M., Spain, T. G., and Ampe, C.: Diurnal, synoptic and seasonal variability of atmospheric CO_2 in the Paris megacity area, Atmos. Chem. Phys., 18, 3335-3362, https://doi.org/10.5194/acp-18-3335-2018, 2018.

Yang, S., Kong, F., Yin, H., Zou, J., Järvi, L., and Sun, J.: Short-term responses of urban forest carbon dynamics to combined heatwave and drought in subtropical China, Agr. Forest Meteorol., 372, 110728, https://doi.org/10.1016/j.agrformet.2025.110728, 2025.

Yi, Z., Fu, S., Yi, W., Zhou, G., Mo, J., Zhang, D., Ding, M., Wang, X., and Zhou, L.: Partitioning soil respiration of subtropical forests with different successional stages in south China, Forest Ecology and Management, 243, 178-186, https://doi.org/10.1016/j.foreco.2007.02.022, 2007.

Zhang, J., Liang, Y., Pei, C., Huang, B., Huang, Y., Lian, X., Song, S., Cheng, C., Wu, C., Zhou, Z., Li, J., and Li, M.: Atmospheric CO_2 dynamics in a coastal megacity: spatiotemporal patterns, sea–land breeze impacts, and anthropogenic–biogenic emission partitioning, Atmos. Chem. Phys., 26, 3253-3276, https://doi.org/10.5194/acp-26-3253-2026, 2026.

Zhang, K., Gong, Y., Fa, H., and Zhao, M.: CO_2 Flux Characteristics of Different Plant Communities in a Subtropical Urban Ecosystem, Sustainability, 11, 4879, https://doi.org/10.3390/su11184879, 2019.

Zhang, X., Liu, L., Zhao, T., Zhang, W., Guan, L., Bai, M., and Chen, X.: GLC_FCS10: a global 10 m land-cover dataset with a fine classification system from Sentinel-1 and Sentinel-2 time-series data in Google Earth Engine, Earth Syst. Sci. Data, 17, 4039-4062, https://doi.org/10.5194/essd-17-4039-2025, 2025.